Renewable Energy 256 (2026) 124698

Contents lists available at ScienceDirect

Renewable Energy

journal homepage: www.elsevier.com/locate/renene

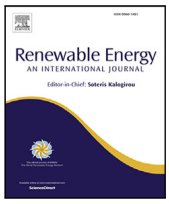

Role of preload in determining the performance enhancement of tidal turbines by passive pitch

Puja Sunil [a], Kuba Frankowski [a], Anna M. Young [b], Michael O'Sullivan [c], Edward D. McCarthy [c], Riccardo Broglia [d], Ignazio Maria Viola [a,*]

[a] The University of Edinburgh, School of Engineering, Institute for Energy Systems, Edinburgh, EH9 3FB, Scotland, United Kingdom
[b] Department of Mechanical Engineering, University of Bath, Bath, BA2 7AY, England, United Kingdom
[c] The University of Edinburgh, School of Engineering, Institute for Materials and Processes, Edinburgh, EH9 3FB, Scotland, United Kingdom
[d] Institute of Marine Engineering, National Research Council, Via di Vallerano 139, Rome, 00128, Italy

ARTICLE INFO

Keywords:
Tidal turbines
Passive pitch
Hydrodynamic efficiency
Thrust
Power
BEMT

ABSTRACT

In this study, we present results from an experimental and analytical study on a turbine equipped with three independent passively pitching blades and show the effect of different levels of spring preload. Results demonstrate that passive pitch blades can produce the same power and thrust as a fixed pitch turbine at any design condition. If the preload is set below the optimum value, the power captured is reduced, but the thrust load is reduced by a larger amount, leading to an increase in hydrodynamic efficiency. Setting the preload too high results in increased thrust and reduced power at the turbine design point. At off-design conditions, the passive pitch turbine with optimal preload shows reduced thrust compared with the fixed pitch turbine while matching the power output, giving an efficiency increase of up to 20%. Therefore, passive pitch can be used to improve efficiency when working at off-design conditions. The passive pitch system is also shown to mitigate load fluctuations at frequencies below the turbine rotational frequency. Results from the analytical study show that blade element momentum theory can be used to model the dynamics of a passive pitch turbine, and it is therefore an appropriate design tool for such systems.

1. Introduction

Tidal stream energy is a reliable and sustainable source of renewable energy that can contribute towards energy security [1]. The slow variations in tidal flow velocity are highly predictable; for example, the semi-diurnal lunar constituent has a period of 12.42 h. However, the rate of installation of renewable energy devices, such as tidal turbines, is limited due to challenges related to system reliability, maintenance, and survivability [2]. At one of the most energetic tidal sites, the Pentland Firth, the tidal velocity varies from more than 5 m s^{-1} in one direction to the same amount in the opposite direction twice a day [3].

Tidal turbine blades also experience large unsteady load fluctuations over shorter time scales, for example, due to flow unsteadiness, wave-induced current [4], turbulence, yaw and shear of the oncoming flow [5], which may lead to fatigue failure. In addition, variations in blade loading may arise due to interactions with neighbouring turbines, as has been shown numerically [6] and experimentally [7], angular velocity fluctuations, tower passing perturbations, and flow-induced structural vibrations.

In order to operate over a wide range of conditions, many turbines adopt an active collective pitch control system that allows all the blades to pitch simultaneously to maintain the rated power despite changes in inflow velocity [8]. As an advancement on this, individual pitch control, where each blade can move independently from the other blades can give additional benefits from loading due to rotating through non-uniform flow such as that due to the atmospheric or seabed boundary layer [9].

In addition to pitching the entire blade, several active control strategies have been employed to mitigate higher frequency load fluctuations. These strategies include trailing edge [10], flaps [11], leading edge slats [12], and microtabs [13]. Numerical simulations on a 5 MW wind turbine showed that trailing-edge flaps can decrease fatigue loads [14]. Furthermore, experiments conducted on a model-scale tidal turbine with wave-induced unsteady inflow showed that actively controlled trips have the potential to reduce unsteady torque fluctuations, while actively controlled flaps give an attenuation in thrust fluctuations [15]. However, all active control systems introduce additional mechanical complexity and communication requirements, and this complexity can increase the potential for failure [16].

* Corresponding author.
E-mail address: i.m.viola@ed.ac.uk (I.M. Viola).

https://doi.org/10.1016/j.renene.2025.124698
Received 16 May 2025; Received in revised form 3 October 2025; Accepted 28 October 2025
Available online 3 November 2025

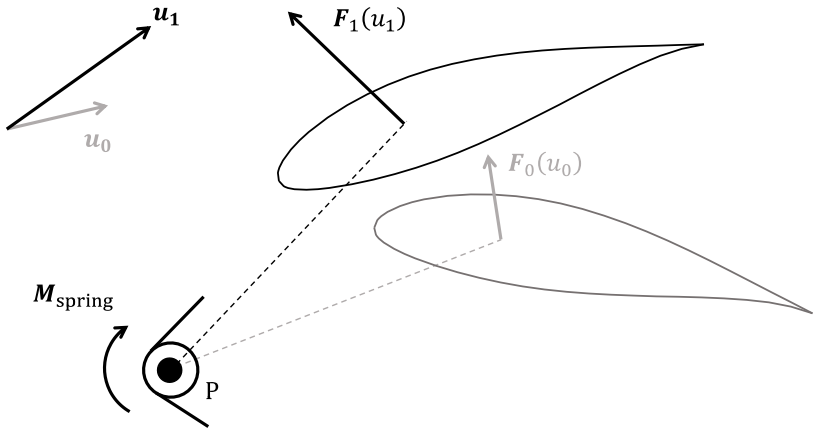

Fig. 1. A schematic of a blade section passively pitching about the pivot point P after a change in the free stream flow velocity from u_0 to u_1.

To address these concerns, there has been an increased focus recently on developing passive control mechanisms to mitigate unsteady load fluctuations. Passive control can be realised in two ways: (1) modifying the blade section camber, or (2) introducing changes in the blade twist, known as aeroelastic tailoring.

At the blade section level, adaptive camber aerofoils have been shown to reduce load fluctuations from gusts, while generating more mean lift than a rigid aerofoil [17]. On a full rotor, bio-inspired hyperflexible turbine blades have been shown to reduce flow separation and stall, thus reducing structural loads [18]. Passive adaptive blades have also been shown to be useful for power capping at inflow speeds higher than rated: experiments by Van Ness et al. [19] showed that passively adaptive blades could produce constant torque at flow speeds up to 14% above rated. As a less mechanically complex alternative, the blade camber can be modified by means of a freely moving flap [20]. Arredondo-Galeana et al. [21] demonstrated that a passively pitching trailing edge flap can mitigate unsteady loads by a fraction proportional to the ratio of the flap length to the chord length. Passive adaptive blades with bend-twist coupling reduce load fluctuations by twisting towards feather when a gust causes increased loading, and away from feather when the loading reduces. The effectiveness of this approach has been shown in towing tank tests by Murray et al. [22].

A passively pitching foil can be thought of as either a passive flap covering 100% of the chord, or an adaptive twist applied simultaneously over the whole blade span, and so an otherwise rigid blade can respond to changes in inflow. The benefits of passive morphing described above can thus be achieved by employing a relatively simple mechanism attached to the root section of the blade. Passive pitch can be achieved by applying a constant torque to the root of the foil, for example, by means of a torsional spring. This is illustrated in Fig. 1, which shows a change in pitch angle between two flow conditions ($\boldsymbol{u}_0$ and $\boldsymbol{u}_1$). A steady blade pitch position is one that produces an equilibrium between the spring moment ($\boldsymbol{M}_{\text{spring}}$) and the moment due to the hydrodynamic force ($\boldsymbol{F}_0$ and $\boldsymbol{F}_1$).

Viola et al. [23] first introduced and conceptualised a passive pitch mechanism for thrust and power control in tidal turbines. This work was followed by a theoretical study by Pisetta et al. [24] that explains the underlying mechanism of morphing blades. The authors showed that a blade that can passively and elastically pitch can completely cancel the thrust fluctuations without affecting the mean power. This concept was investigated analytically and numerically on a full-scale turbine in a sheared flow by Dai et al. [25]. Here, each blade was connected to the hub by means of a torsional spring, allowing the blades to pitch passively. This study showed that a turbine equipped with passive pitching blades can reduce rotor thrust fluctuations by nearly 80%.

Ōtomo et al. [26] demonstrated that the optimal pivot point can be computed analytically with a quasi-steady approach. They also developed a low-order model including added mass and quasi-steady forces, revealing that the optimal pitching location depends on the inertia of the blade. Liu et al. [27] demonstrated numerically that a passively pitching foil with a pitching axis located upstream of a pitching foil can mitigate load fluctuations by nearly 80% even for extreme freestream flow velocity variations.

Gambuzza et al. [28] were the first to demonstrate experimentally the effectiveness of morphing blades in mitigating thrust and torque fluctuations on a 1.2 m diameter turbine in the Flowave Ocean Energy Research Facility. They showed that fluctuations in torque, thrust and root bending moment were reduced over a broad range of tip-speed ratios. However, in their study, the pitch axis was inside the blade, resulting in a relatively low spring moment. This, together with a relatively high friction at the bearing, might have reduced the potential unsteady load mitigation of the passive pitch system.

In a subsequent study with a different set of blades and pitch system design, Gambuzza et al. [29] tested a pivot location about one chord upstream of the blade. They showed that it is possible to match the power of a fixed-pitch turbine for a given flow speed and angular velocity. Furthermore, the passive pitch system results in a constant thrust over an extensive range of freestream speeds. They also showed that power can be capped by changing the turbine angular velocity, and that thrust and power are minimally affected by yaw misalignment if passive pitch is employed. Finally, they showed that the quasi-steady performances of the passive pitch system are well predicted by a low-order model based on Blade Element Momentum Theory (BEMT). However, this second study of Gambuzza et al. [29] did not consider the mitigation of high-frequency fluctuations because tests were undertaken in a low-turbulence facility with negligible shear along the water height.

While passive pitch systems have been widely demonstrated by Gambuzza et al. [28,29], none of the previous studies have explored the effect of spring preload. Furthermore, whether a low-friction passive pitch design with a longer arm between the blade and the pitching axis than the one tested by Gambuzza et al. [28] allows higher unsteady load mitigation is yet to be proven. Finally, the ability of BEMT to predict the system response to high-frequency load fluctuations is also not known. Therefore, this paper aims to address the following questions: (1) What is the effect of spring preload on the performance of a turbine with a passive pitch system? (2) Over what range of frequencies are load fluctuations mitigated by passive pitch? (3) Can a BEMT code be used to model such a system in a turbulent sheared flow?

The rest of the paper is organised as follows. The turbine and the facility are described in Section 2. The BEMT model is described in Section 3. The results of the experimental tests and of the BEMT simulations are presented in sections 4.1 and 4.2, respectively, and the main conclusions are summarised in Section 5.

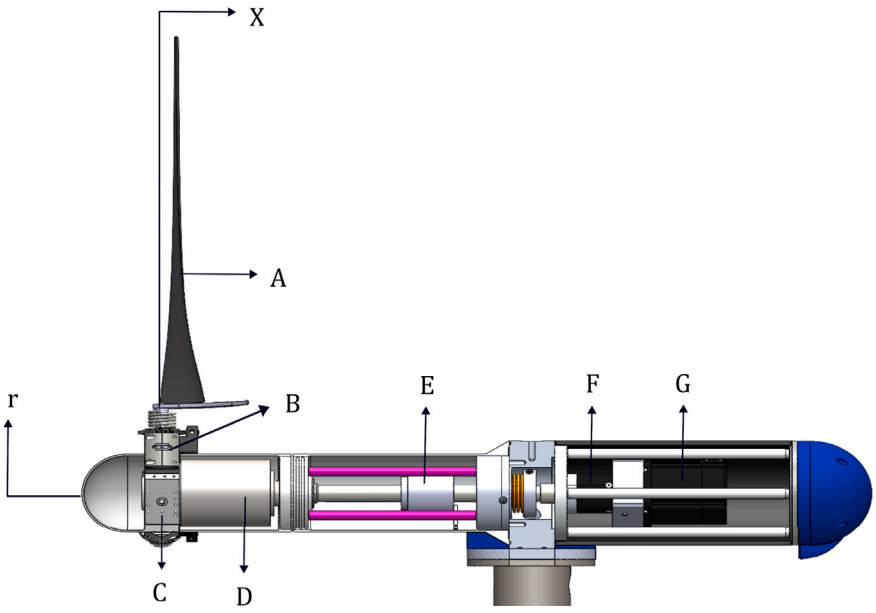

Fig. 2. Schematic of the turbine assembly showing different components: (A) turbine blades, (B) passive pitch mechanism, (C) turbine hub, (D) thrust torque transducer, (E) slip ring, (F) gearbox, (G) brushless DC motor.

2. Experimental details and turbine geometry

2.1. Facility

The experiments were conducted in the University of Edinburgh's Flowave Ocean Energy Research Facility, which is a wave and current tank designed for research related to tidal energy applications. The tank is circular, with a diameter of 25 m and depth of 2 m, and can generate flow speeds of up to 1.6 m s^{-1}. Far stream flow velocities were measured using Acoustic Doppler Velocimetry (ADV). For the tests described in this paper, the turbulence intensity was found to vary from 6.1 to 7% and the vertical velocity profile in the tank followed a power law described as,

$$\frac{u}{u_{\text{hub}}} = \left(\frac{z}{z_{\text{hub}}}\right)^{n} \tag{1}$$

where z is the vertical direction, with origin at the tank floor. z_{hub} is 1 m from the tank floor, and the shear exponent n is reported by the facility to be approximately 1/15 close to the tank centre [30]. An ADV characterisation repeated at the experimental location and flow conditions used in the turbine tests, however, reported a value closer to 1/10. The characterisation process is described in further detail in Section 3.1.1. Both the freestream turbulence and the vertical velocity profile will induce unsteady relative inflow onto the turbine blades as they rotate. The turbine hub centre and the blade tip were located at 1 m and 0.305 m from the water surface, respectively.

2.1.1. Turbine geometry and pitch system

The model-scale turbine nacelle and sensors used in this facility are those used by Gambuzza et al. [29]. The main components of the turbine are outlined in Fig. 2, where we define the coordinate system used in this work. This is a cylindrical reference frame, having its origin at the centre of the turbine hub on the rotor plane. Distance along the turbine rotor axis is represented by X, the radial coordinate is represented by r, and the polar coordinate is denoted by ψ.

The blades are an 80%-scale version of the blades used in the Supergen Tidal Turbine Benchmarking Project (referred to as the Benchmarking Turbine) and documented in [2]. However, there are differences in blade mounting arrangement between the present tests and the Benchmarking Turbine. For the Benchmarking Turbine, the blades are directly mounted on the turbine hub, and the root of the blade fits the circular shape of the hub. Conversely, in the present work, the blades are cut straight at the root and connected through a lever arm to the axis of a passive pitch mechanism, which is mounted on the turbine hub (Fig. 2). The hub diameter is 70 mm, while the radial coordinate of the root and tip of the blade are 135 mm and 695 mm, respectively. Overall, the diameter of the rotor is 1.39 m. Each section of the blade is made of a NACA 63-415 aerofoil. The blades are made of a 3 mm carbon fibre reinforced polymer (CFRP) skin and a stainless steel metal insert, which connects onto the lever arm of the passive pitch system.

An exploded view of the pitching mechanism is shown in Fig. 3. The turbine blade, A, is mounted on a lever arm, B. The lever arm sets the spacing between the blade and the pitching axis, E. The rotation of the pitching axis is constrained by two components: a torsional spring C and a retention and limiting screw, I. The torsional spring is connected to the lever arm at its top end, and to a spur gear, D at its bottom end. The spur gear connects to a worm gear, K, which controls the rotation of the spur gear. The worm gear is secured to a frame, J by means of a bolt. The worm gear can be rotated manually by means of a key, which consequently turns the spur gear, and thereby the bottom leg of the spring, thus setting the preload of the spring. The rotation of shaft E is limited by the retention and limiting screw, I, which is engaged on the threaded hole in the shaft: as the shaft rotates, the screw moves in a slot cut in the two frame halves, F, within a range of 25° in each direction. The screw can also be fastened until its head engages on a flat surface cut on the frame half, F, thus disabling the passive pitch mechanism to enable fixed pitch testing.

The pitching system allows the blade to pitch around a radial axis. The position of the pitching axis with respect to the blade was chosen using the method outlined in [26]. As discussed by [31], different positions of the pitching axis allow the designer to prioritise the mitigation of either the torque or the thrust fluctuations. In general, the optimum pitching axis is upstream of the blade and towards the pressure side. The optimum distance from the blade depends on the inertia, with the optimum pitching axis for a heavier blade being nearer to the blade. However, the level of unsteady load mitigation does not vary significantly with the exact location of the pitching axis. For this paper, the pitching axis was located 10 mm upstream of the quarter-chord location along the chord of the root section, and 18 mm towards the pressure side in the chord-normal direction. The effect of the position of the pitching axis will be discussed in Section 4.2.4.

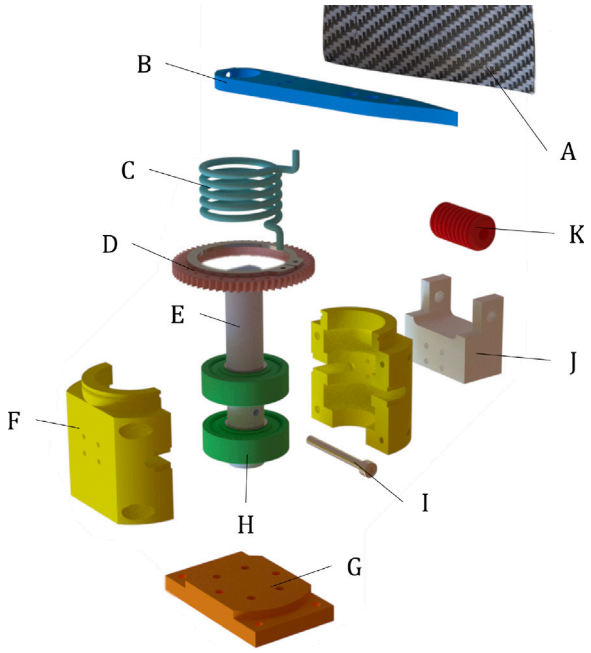

Fig. 3. Exploded view of the pitching mechanism. (A) Turbine blade, (B) lever arm, (C) torsional spring, (D) spur gear, (E) pitching shaft, (F) frame, (G) mounting plates, (H) ball bearings, (I) retention and limiting screw, (J) preload worm mounting frame, (K) worm gear.

The rotation of the blade about the pitching axis is constrained by a torsional spring, which can be preloaded manually by turning a worm gear. The preload is chosen to balance the time-averaged hydrodynamic pitching moment at the design flow speed and tip-speed ratio. This ensures that the mean pitch is equal to the design pitch of the corresponding rigid blade configuration, and thus that both the passive pitch and the fixed pitch blades should deliver the same mean torque and thrust at the design condition. In this work, the design pitch is taken as the unpitched position of the fixed pitch blade. Thus, blade pitches β are measured as the angular displacement from this position where $\beta = 0°$. Negative pitches reported in this paper imply a nose-up motion (towards stall), and positive as feathered into the flow. The torsional spring used in these tests is made of stainless steel and has a diameter of 2.05 mm. Assuming a Youngs modulus of 200 GPa, the spring stiffness, κ, is estimated to be $0.31\,\mathrm{N\,m\,rad^{-1}}$.

The turbine hub is mounted on a force–torque sensor. The signals from the sensor are transferred through a slip ring assembly to a data acquisition board. The turbine is driven by a Nanotech brushless DC motor (rated power: 534 W, rated torque: 0.17 N m), with speed control provided by an ESCON 70/10 servocontroller. The speed is set using a voltage demand to the motor and monitored using an encoder. The motor can be used in motor or generator mode, i.e. driving the turbine or acting as a brake.

The turbine is designed to operate at a freestream speed, u_∞ of $0.65\,\mathrm{m\,s^{-1}}$, and was tested with u_∞ of $0.5\,\mathrm{m\,s^{-1}}$ and $0.65\,\mathrm{m\,s^{-1}}$, resulting in diameter-based Reynolds numbers, $Re \equiv u_\infty d/\nu$ of 0.90×10^6 and 1.17×10^6, respectively.

In the present study, we tested two blade configurations: (1) Fixed pitch blades, and (2) Passive pitch blades. The fixed pitch blades are the same blades, but with the passive pitch mechanism locked in the datum position.

2.1.2. Data acquisition and reduction

The thrust and torque data were measured using an Applied Measurements DBBSS-TSF torque and axial force sensor installed between the turbine rotor and the motor shaft and rated for an axial load of 1300 N and torque of 100 N m. The measured data were therefore the net force and torque generated by the rotor and not by individual blades. The transducer outputs current signals in the range of 4 mA to 20 mA, which are then converted to thrust and torque signals using the calibration data provided by the manufacturer. The wires carrying thrust and torque signals are passed through a slip ring to the data acquisition hardware. Data was acquired through a National Instruments NI 9203 data acquisition board at a sampling rate of 128 Hz for a duration of 120 s.

The oncoming flow velocity in the tank was measured by ADV, using Nordec's Vectrino, at 100 Hz with a 120 s sampling period. During the experiments, the Vectrino was placed at hub height and 1.65 D upstream of the turbine hub centre. Velocity was measured both during and after the tests in order to ensure that the velocity was constant at the set value. The Vectrino was also used to measure the water temperature in the tank and to estimate the fluid density and kinematic viscosity according to the relations in [32,33].

Thrust and torque data were acquired at different conditions of oncoming flow velocity and tip-speed ratio. Here, the tip-speed ratio is defined as,

$$\lambda \equiv \frac{\omega R}{u_\infty}, \tag{2}$$

where ω is the turbine angular velocity, and R is the turbine radius. For the present experiments, the turbine angular velocity was varied to obtain tip-speed ratios of λ = 3, 3.5, 4, 4.5, 5, 5.5, 6, 7, 8 at each value of u_∞. Here, thrust is defined as the net streamwise force generated by the blades along the X direction, and torque is the moment of the net force generated by the blades in the ψ direction. Thrust and power are expressed in non-dimensional form as,

$$C_T \equiv \frac{T}{\frac{1}{2}\rho u_\infty^2 \pi R^2}, \tag{3}$$

and

$$C_P \equiv \frac{P}{\frac{1}{2}\rho u_\infty^3 \pi R^2}, \tag{4}$$

where the mechanical power generated by the turbine is given by $P = Q\omega$.

3. Numerical methods

3.1. BEMT

The turbine used in the experimental study described above has also been modelled using Blade Element Momentum Theory (BEMT). BEMT is a method used to estimate aerodynamic forces acting on a rotor by considering the momentum and energy changes within a fluid volume between the far field, the rotor, and the turbine wake [34]. The energy and momentum changes are coupled with the aerodynamic forces acting on each blade, itself split into individual spanwise elements for which lift, drag and pitching moment characteristics are known. Given a flow speed u_∞, fluid density ρ and a blade geometry, BEMT can be used to calculate the corresponding loads on each blade element, which are then integrated over the span of the blade to calculate the total loading on each blade, and when repeated for each blade, the total loading on the rotor.

The software used in this study was OpenFAST [35], a multi-physics tool used for calculating loads on wind and tidal turbines. OpenFAST's BEMT module AeroDyn [34] can take as inputs different flow conditions by specifying flow profiles, such as a uniform flow of a single velocity u_∞, or a time and height-varied shear flow described by Eq. (1). Having information about local flow conditions, OpenFAST can accordingly calculate loads at each blade section, at each azimuthal position and time step.

Prandtl's corrections for hub and tip losses are applied [36]. As BEMT considers the aerodynamic properties of the blades only, the thrust and torque contributions as experienced by the hub section of the rotor itself are not considered.

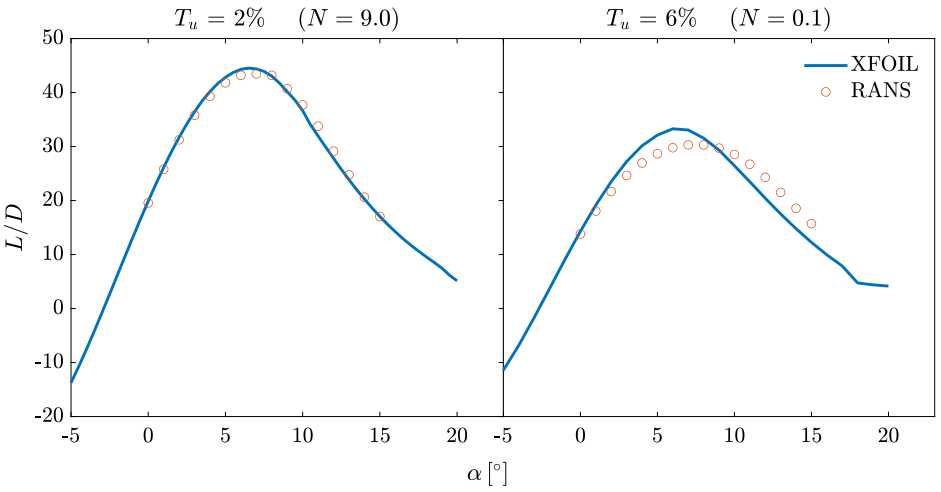

Fig. 4. Lift-over-drag ratio versus the angle of attack computed using XFOIL and RANS simulations for a blade section at 75% of the blade span for $\lambda = 5.0$ and $u_\infty = 0.65$ m s^{-1}. Turbulent intensities are given with a corresponding transition factor N.

3.1.1. Hydrodynamic modelling of the turbine

A program was written [37] for generating AeroDyn-compatible aerodynamic polars using XFOIL [38] and AirfoilPreppy [39]. An estimate of the sectional Reynolds number for a rotating turbine is calculated as

$$Re = \frac{c(r)\,u_\infty}{\nu}\sqrt{1+\left(\frac{r}{R}\lambda\right)^2}, \tag{5}$$

accounting for the speed contributions from the fluid and rotational motion of the blade, blade geometry using the chord lengths c, and fluid properties using its kinematic viscosity ν. The corresponding Re and sectional aerofoil geometries are then input into XFOIL, which generates aerodynamic coefficients for a range of angles of attack. The coefficient for sectional lift L is calculated as

$$C_L \equiv \frac{L}{\frac{1}{2}\rho\, c\, u_{\text{rel}}^2}, \tag{6}$$

using the relative sectional flow velocity u_{rel}, arising from the rotational motion of each blade section. The process is also used to calculate the coefficient given a drag D. The coefficient of the aerodynamic pitching moment expressed at the quarter chord length M is defined as

$$C_M \equiv \frac{M}{\frac{1}{2}\rho\, c^2\, u_{\text{rel}}^2}. \tag{7}$$

Fig. 4 shows a comparison between non-dimensional force coefficients generated using XFOIL and Reynolds Averaged Navier Stokes (RANS) simulations, which show good agreement across common angles of attack α. The RANS results have been supplied for the turbine benchmarking project using the same aerofoils [2].

Two plots are shown for two values of the turbulence intensity, T_u, defined as the ratio of the standard deviation σ_u to the far stream flow speed u_∞. Higher T_u is modelled in XFOIL for a given Reynolds' number by setting a lower turbulent transition factor e^N [40], as seen in Fig. 4.

The RANS results were generated and provided for the benchmarking study by the authors of the original turbine geometry [2], as used in this paper. A limitation of XFOIL, as seen in the figure, is in the range of α that it can analyse. Being based on boundary layer theories [38], the program is capable of predicting the onset of flow separation; however, at α beyond stall, XFOIL becomes incapable of converging to physical solutions.

This limitation, however, is of little relevance of this project as results later presented in Section 4.2.3 will show that within the operational range of the turbine, the blades are not stalled. Although the transition to and from stall is an important consideration in studying the operational limits of turbine pitching systems, a turbine would not be expected to operate beyond stalled conditions. Therefore, the need for accurate sectional data in stall is beyond the scope of this work.

3.1.2. Modelling of passive pitch

The dynamics of the passive pitch controller were modelled within Simulink [41], considering the blade as a driven harmonic oscillator. The equation of motion,

$$I\ddot{\beta}(t) + \mu(t)\dot{\beta}(t) + \kappa\,(\theta + \beta(t)) = M_h(t), \tag{8}$$

takes time-constant parameters: I, the total inertia of the pitching system model; and spring stiffness κ. The hydrodynamic pitching moment at the root of each blade $M_h(t)$ is taken as an output from OpenFAST for each time-step t, and input into the model to calculate the resultant change in pitch β, while θ is the spring preload (given as the initial spring pre-coiling). The significance of preload is described in further detail in Section 3.1.3.

Dynamic effects of the system are based on Theodorsen's theories of unsteady aerodynamics [42]. Added mass is considered, given as the term acting on the second time derivative from Theodorsen's pitching moment equation, taking the form of an added inertia I_{added},

$$I_{\text{added}} = \int_{r_{\text{hub}}}^{R} \frac{1}{16}\rho\, c^4 \left(\frac{1}{8} - a^2\right) \mathrm{d}r, \tag{9}$$

giving a total inertia on the system,

$$I = I_{\text{blade}} + I_{\text{added}}. \tag{10}$$

Added inertia is calculated over the span of the blade, from the hub radius r_{hub} to the rotor tip at R, by integrating the density of the fluid ρ and sectional chord lengths c at all spanwise blade positions r. A term a is also seen, which describes the positions at which inertia is computed, and is given as a fraction of a half-chord b. In this case, the moment of inertia is calculated around the quarter chord of the root section of the blade $a = -1/2$, where the pitching arm connects between the blade to the blade pitching axis. Effects of the pitching axis being located upstream of the blade, separated from the root quarter chord by a distance r_{p} and an angle θ_0, are modelled using the parallel axis theorem.

Having an offset pitching axis will also affect the net hydrodynamic pitching moment. By default, pitching moments are output from BEMT at the quarter chord location of the blade, $M_{1/4}$. A total pitching moment around an offset pitching axis can be calculated by the sum of this moment and the cross product between the lever arm vector $\boldsymbol{r}_{\text{p}}$ and the forces acting at the quarter chord location $\boldsymbol{F}_{1/4}$,

$$\boldsymbol{M}_{\text{h}} = \boldsymbol{M}_{1/4} + \boldsymbol{r}_{\text{p}} \times \boldsymbol{F}_{1/4}. \tag{11}$$

The second unsteady term considered is the hydrodynamic damping, which is calculated as the difference between the non-circulatory and circulatory moment coefficients around each blade section,

$$\mu(t) = \int_{r_{\text{hub}}}^{R} \left(C_{nc}(t) - C_c(t)\right) \, \mathrm{d}r. \tag{12}$$

The moment coefficients are calculated as

$$C_c = -\rho\, u_{\text{rel}}\, b^3 \pi \left(\frac{1}{2} - a\right) \left(1 + 2a + 2\frac{\dot{h}}{b\,\dot{\alpha}}\right) C(k), \tag{13}$$

$$C_{nc} = -\rho\, u_{\text{rel}}\, b^3 \pi \left(\frac{1}{2} - a\right), \tag{14}$$

where $C(k)$ is Theodorsen's circulation function, expressed in terms of Henkel functions of the second kind, and is a function of the reduced frequency,

$$k = \frac{\dot{\alpha} b}{u_{\text{rel}}}. \tag{15}$$

For an offset pitching axis, the pitching motion will be accompanied by a vertical translation, also referred to as heaving. Its contribution is contained in the $\dot{h}$ term, which will depend on the geometry of the lever arm.

Additional damping can be expected to act on the system due to, for example, the friction of the ball bearings within the pitching mechanism [43]. The damping of the ball bearings used in the experiment has been characterised by oscillating the pitching mechanism and tracking the angular position of the lever arm without the presence of a blade. Knowing the inertia and spring stiffness of the pitching system, a damping coefficient could be estimated by fitting the solution for a damped harmonic oscillator. The bearing friction was found to be over two orders of magnitude smaller than the hydrodynamic damping from Eq. (12), and has therefore been considered negligible and not included in the model.

3.1.3. Spring preload

The primary objective of this paper is to demonstrate the effect of spring preload on the response of the turbine to varying flow conditions. A critical component of the mechanism of passive pitch, the preload sets the mean spring moment that opposes the hydrodynamic pitching moments. The time-averaged form of Eq. (8) gives

$$\kappa\,(\theta + \beta) = \bar{M}_h, \tag{16}$$

which shows that the mean spring moment balances the mean hydrodynamic moment, $\bar{M}_h$, given by the time-averaged of Eq. (11).

The sum of θ and β represents the total coiling of the spring. As will be shown in Section 4, the stiffness κ and the preload θ set the operating point (u, λ) at which a passively pitching turbine matches the performance of a fixed-pitch counterpart.

A given spring preload moment can be set with different combinations of the two variables κ and θ. Previous studies on the effect of spring stiffness have shown that effective load mitigation is achieved with low κ and high θ [44], such that the spring moment remains approximately constant for small changes in blade pitch angle, β. An optimum stiffness minimising root-bending moment fluctuations was reported by Pisetta et al. [24] using a non-dimensional stiffness coefficient

$$C_\kappa = \frac{\kappa}{\rho \pi R^2 u_\infty^2 c^2}, \tag{17}$$

in the order of 10^{-2}. This result is consistent with the present work, where the optimum C_κ is also found of the order of 10^{-2} with BEMT simulations. The reduction in the root bending moment fluctuations versus C_κ is shown in Fig. 5 for the present turbine when rotating in a steady sheared flow. The optimal stiffness is $\kappa = 0.31\,\text{N m/rad}$, corresponding to $C_\kappa \approx 6.9 \times 10^{-3}$. Given these spring parameters and the flow conditions of the experiments, Eq. (16) is satisfied for θ of the order 100°. Within the present study, θ is varied by ±50% during experiments.

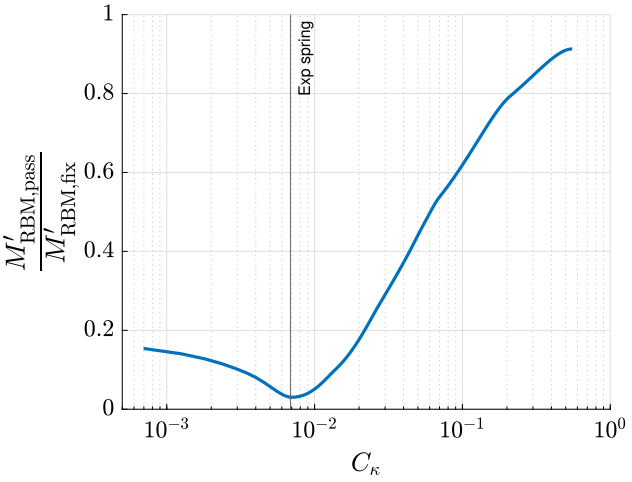

Fig. 5. Ratio of root-bending moments obtained using BEMT between a passively pitching and fixed pitch turbine, rotating in a steady sheared flow.

3.1.4. Modelling flow data

Real flow conditions measured at the experimental facility have been used as inputs for the numerical model. Measurements collected using ADVs can be prone to noise and signal interference. Fitting the data to a turbulent spectrum can thus be used to reconstruct the original signal associated with the flow and regain otherwise lost information hidden by noise. Measured flow fluctuations u', calculated as the difference between the time–history of the flow, u, and its mean, $\bar{u}$, have been fitted to a Von Kármán spectrum $S(f)$ of the form

$$S(f) = \frac{4\sigma_u^2 L/\bar{u}}{\left(1 + 70.8\left(Lf/\bar{u}\right)^2\right)^{5/6}}. \tag{18}$$

The two fitting parameters are the standard deviation of the fluctuations in u, σ_u, and the turbulent length scale L. They have been solved for using Matlab's `fminsearch` function by minimising the difference between measured and fitted spectra, $S(f)$. Using the newly fitted $S(f)$, a time series of flow fluctuations can be reconstructed to create a turbulent flow time series that can be used as an input for the numerical model. Fig. 6 compares the spectra of the experimental fluctuations (blue), reconstructed signal (red) and the fitted von Kármán curve (black). The fitted spectrum is in good agreement with the experiment at frequencies between 10^{-1} and 1 Hz. For frequencies above 1 Hz, the plots show a clear divergence between the measured signal and that expected for a real, turbulent flow, suggesting that low-energy turbulence measured using ADV was obfuscated by signal noise.

The flow input for the model was expressed on a two-dimensional grid, created using TurbSim [45]. TurbSim is software capable of taking user spectral parameters, σ_u and L, and the vertical shear profile to generate unique, stochastic time series over an area. Such a flow field is capable of preserving experimentally informed flow statistics, spatial and temporal, allowing it to more accurately mirror the flow of real experimental conditions, compared to a single input flow. For instance, a simpler approach would be to generate a flow time series at a single location, and extrapolate the flows by scaling them according to the shear law, seen in Eq. (1). Flow fluctuations along the height of the rotor would therefore share the same phase and be synchronised, resulting in a pulsed loading on a turbine, uncharacteristic of real turbulent flows. A temporal and spatial statistical representation of a flow obtained using a program such as TurbSim, where local phases are stochastically generated to preserve the coherent structures within the flow, would therefore be more suitable in modelling the turbulence present in the experiment. Fig. 7 shows a snapshot at a single time step of the flow-grid used in the numerical simulations. The grid spacings used in the model were set to be equal to the average chord length of

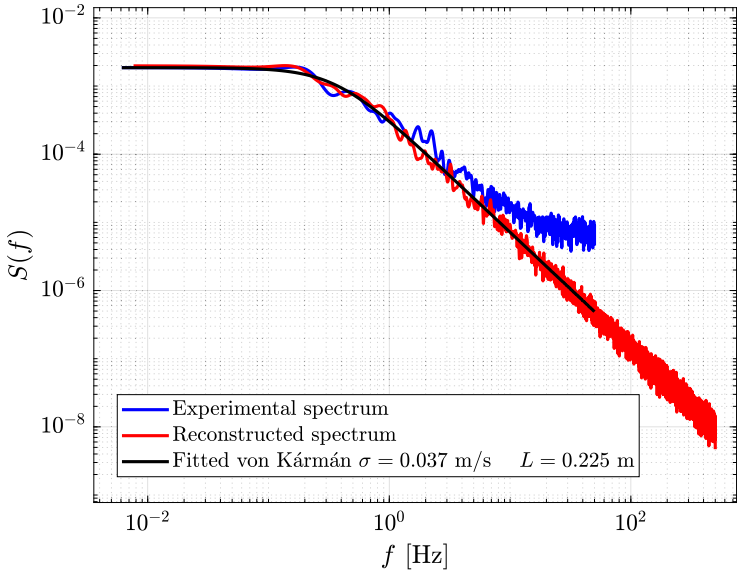

Fig. 6. Non-dimensional forms of fitted von Kármán spectrum and power spectrum density of the experimentally measured fluctuations.

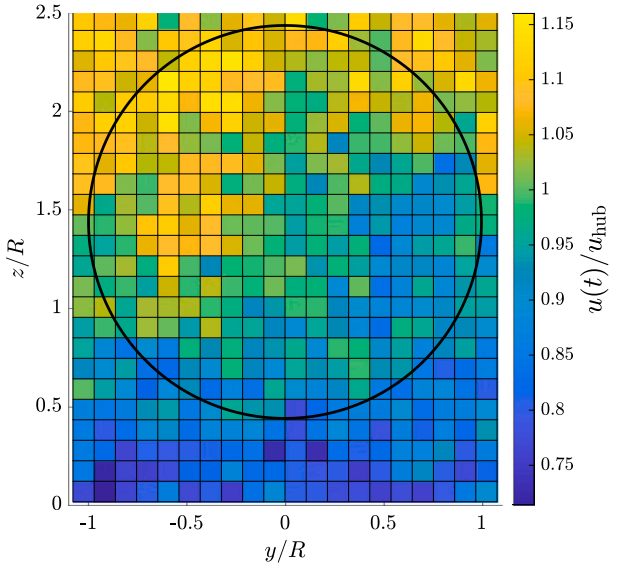

Fig. 7. Two-dimensional flow grid used in simulations shown for a single time step. The spatial dimensions are shown as ratios of the rotor radius R, with the flow speed a ratio of the mean flow at hub height u_{hub}.

the rotor blade, for a grid dimension of 21 by 25 points. The rotor area, represented by the black circle on the plot, was covered by 309 points. A flow field was generated for a total simulation time of 120 s to match the duration of each experimental run, at a frequency of 1000 Hz. Flow parameters as measured and used in the model are seen in Table 1.

4. Results and discussion

For each set of measurements, the turbine was tested with fixed pitch and passive pitch blades. For the first set of tests, the oncoming flow velocity was fixed at $u_\infty = 0.5\,\mathrm{m\,s^{-1}}$, while the second set of tests were undertaken with an oncoming flow velocity of $u_\infty = 0.65\,\mathrm{m\,s^{-1}}$. For both sets of tests, the tip-speed ratio, λ, was varied by changing the rotor angular velocity, and the spring preload angle was increased progressively until the power coefficient of the passive pitch blades

Table 1
Experimentally informed flow parameters used to model the numerically generated flow. The parameters are expressed as modelled at hub height z_{hub}. Parameters v' and w' refer to the vertical and spanwise flow fluctuations measured by ADV.

Variable	Value
n	0.096
u_{hub}	0.65 m s^{-1}
σ_u	0.037 m s^{-1}
L_{hub}	0.225 m
$u'v'$	1.798×10^{-6} m^2 s^{-2}
$u'w'$	1.610×10^{-6} m^2 s^{-2}
$v'w'$	1.951×10^{-6} m^2 s^{-2}

matched the maximum power coefficient of the fixed pitch blades. A coarse spacing of tip-speed ratios was set at $\Delta_\lambda = 1$ to cover the range of $\lambda \in [3, 8]$ studied. A finer spacing $\Delta_\lambda = 0.5$ was chosen around the region of matched power. Measurements were taken using these spacings for the fixed pitch turbines, and for passively pitching turbines with the best performing preloads. Non-regular λ spacings and ranges were used to maximise data acquisition across less-favourable preloads within the available time resource. During the present experiments, tests were undertaken with spring preload angles of $\theta = 168°$, $232°$, and $290°$. For $u_\infty = 0.5\,\mathrm{m\,s^{-1}}$ and $0.65\,\mathrm{m\,s^{-1}}$, the optimum spring preload angles were found to be 168° and 290°, respectively, taken as conditions with highest C_P match between the passively pitching and fixed turbines. The experimental results are presented in Section 4.1, and numerical results are reported in Section 4.2.

4.1. Experimental results

The power and thrust performance of the turbine will now be discussed. Considering first the fixed pitch blades (red lines in Fig. 8), it can be seen that the power coefficient is maximised at around $\lambda = 5$ for both inflow velocities tested (Figs. 8a and 8b), while the thrust coefficient increases with λ over the whole range of tip-speed ratios (Figs. 8c and 8d). This behaviour can be explained by considering the velocity triangles in Fig. 9. The tip-speed ratio is increased by increasing the turbine rotational speed, which causes the relative inflow velocity to increase in magnitude and to change direction such that the angle of attack is reduced. The reduction in angle of attack means that

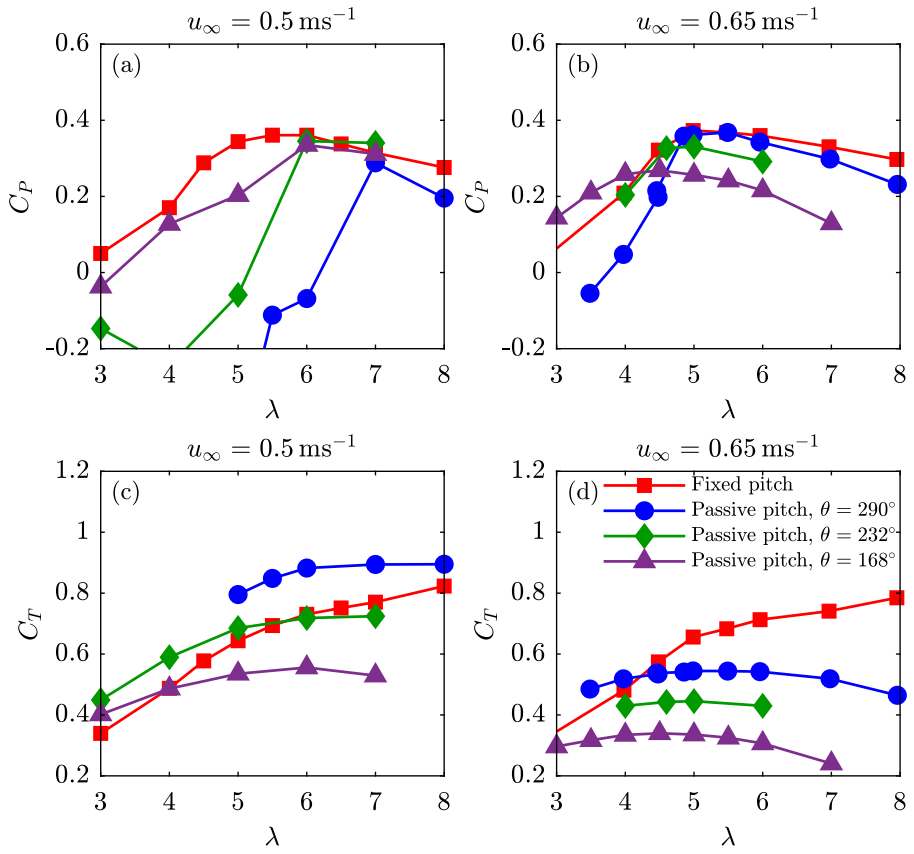

Fig. 8. Power (a, b) and thrust (c, d) coefficients for the fixed pitch rotor and the passive pitch rotor with different preloads and velocities: (a, c) $u_\infty = 0.5\ \mathrm{m\,s^{-1}}$ and (b, d) $u_\infty = 0.65\ \mathrm{m\,s^{-1}}$.

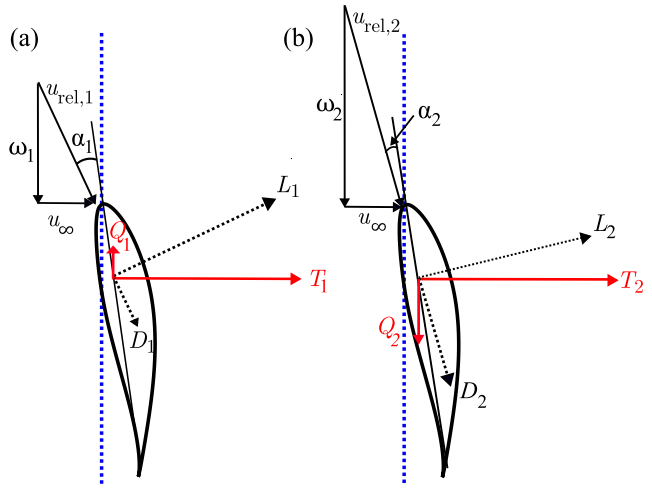

Fig. 9. Velocity triangle demonstrating the effect of tip-speed ratio on the forces acting on a fixed pitch blade section: (a) design λ and (b) high λ.

the lift coefficient reduces (with little change to the drag coefficient, assuming that the flow remains attached), but the increase in relative velocity magnitude counteracts this reduction in lift coefficient to cause an increase in lift force magnitude. The change in inflow direction means that the lift force rotates towards the thrust direction, and the drag force rotates towards the negative torque direction. Overall, these changes cause the thrust coefficient to increase, and the torque coefficient to remain approximately constant at tip-speed ratios near the design point.

Increasing the tip-speed ratio further from the design point ($\lambda > 6$) causes the power coefficient to begin to drop gradually due to the changing balance of the three factors outlined above. Reducing the tip-speed ratio below $\lambda = 4.5$ causes a steep drop in power, due to flow separation causing a more abrupt drop in lift generated on the sections, and a large rise in drag. This drop in lift is also seen in the slightly steeper drop in thrust coefficient at low λ. The performance of the fixed pitch blades is almost identical at the two freestream velocities tested, suggesting limited Reynolds number effects at this scale.

For the passive pitch blades, power and thrust data from tests at three preload angles are shown in Fig. 8. It can be seen that the performance is strongly affected by both freestream velocity and spring preload angle. The effect of tip-speed ratio on the passive pitch blade loading is shown in Fig. 10. At a given operating condition, the blade will rotate about the pitching axis (marked P) until the moment provided by the spring is matched by the hydrodynamic moment on the blade. The passive pitch blades will match the performance of the fixed pitch blades at a given λ if the spring preload is such that the blades pitch to the same angle as the fixed pitch blade. An example of this is seen in the blue curves (θ = 290 °) at u_∞ = 0.65 m s^{-1}, where the power coefficient is matched between the fixed and passive pitch blades. The spring preload of θ = 290 ° is therefore the optimum preload at u_∞ = 0.65 m s^{-1}, because the design point is matched. Reducing the spring preload below this value at $u_\infty = 0.65$ m s^{-1} causes a drop in power, and in thrust, as the blades will pitch more easily than in the optimum case and so they move away from the optimum pitch angle.

For the optimum spring preload at u_∞ = 0.65 m s^{-1}, $C_{P\,\mathrm{passive}}$ matches $C_{P\,\mathrm{fixed,max}}$ at around $\lambda = 4.8$ and again at $\lambda = 5.5$. Over this range of λ, the passive pitch blades rotate to the same angle as the fixed pitch blades, resulting in a match in the lift coefficient parallel to the rotor plane, and therefore, the power. The rotation of the blades

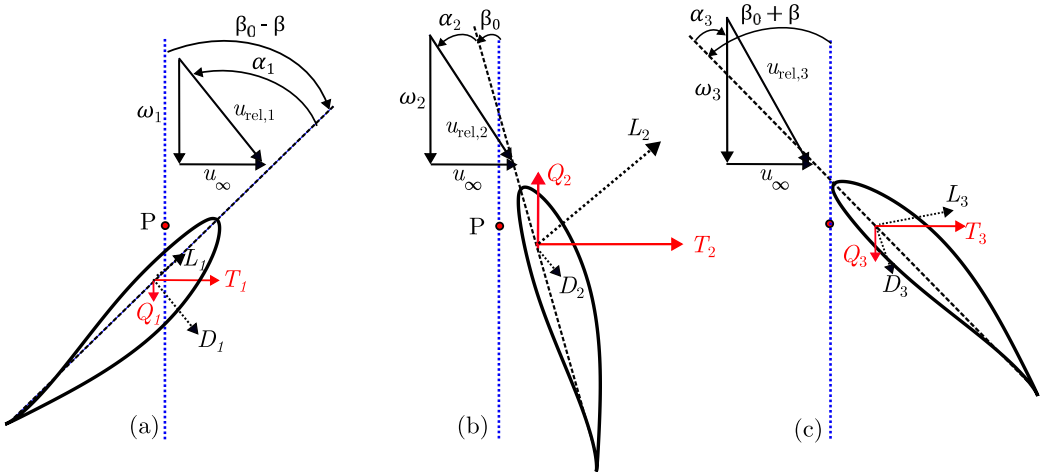

Fig. 10. Velocity triangle demonstrating changes in loading on a blade section undergoing pitching before and after a change in angular velocity: (a) low λ with no end stop, (b) design condition of λ, (c) high λ. The blue dashed line is parallel to the rotor plane. The pitching point, P, is marked as a red dot.

also has implications for the thrust loads experienced by the blades, as discussed in the subsequent paragraph. Outside this optimum range of tip-speed ratios, the power generated by the passive pitch blades is more sensitive to tip-speed ratio than that of the fixed pitch blades. The passive pitch blades are stalled at low tip-speed ratio, resulting in $C_P < 0$ for $\lambda = 3.5$. This indicates that energy is supplied by the motor-generator to drive the turbine, and therefore, care should be taken while designing the passive pitch assembly and setting the maximum and minimum blade pitch angle to ensure that the turbine generates power over the full range of expected tip-speed ratios. In practice, this can be achieved using physical end-stops for the passive pitch mechanism, as discussed in [29] - this approach prevents the blade from adopting the extreme position shown in Fig. 10(a), where negative torque is generated.

For $u_\infty = 0.65$ m s^{-1} and the optimum preload angle, the thrust coefficient of the passive pitch blade $C_{T\ \text{passive}}$ is approximately constant for tip-speed ratios from $\lambda = 4.0$ to 6.0 (Fig. 8(d)). This is in line with the results in [26], where it was shown that the force component along any arbitrary direction can be kept constant if the pivot point lies along a line that depends on the foil characteristics. With an increase in tip-speed ratio, at $\lambda > 4.5$, the blades rotate about the pitching axis, thereby reducing the angle of attack further, becoming more streamlined and presenting less obstruction to the flow. Consequently, the magnitude of the thrust loads experienced by the passive pitch blades is lower than that of the fixed pitch blades, indicating an overall reduction in the structural loads experienced by the turbine.

Considering now the results at the lower inflow velocity ($u_\infty = 0.5$ m/s), Figs. 8a and 8c), it can be seen that a lower spring preload is required to match the performance of the fixed pitch turbine. Power is matched at $\lambda = 6$ for a spring preload of 232 °, and approximately matched at $\lambda = 4$ for a spring preload of 168 °, suggesting that the design point would be matched at an intermediate preload. This result shows that the preload can be tuned to match the performance of a fixed-pitch turbine at a given combination of inflow speed and tip-speed ratio. Importantly, this finding does not mean that the preload must be adjusted for every flow velocity encountered by a turbine, as will be discussed in Section 4.2.4.

Fig. 11 shows the reduction in thrust and power of a turbine equipped with passive pitch blades compared to a turbine with fixed pitch blades. It can be seen that passive pitch enables the mitigation of both the mean and fluctuating thrust loading on the turbine. Reduction in mean thrust loads is particularly sensitive to tip-speed ratio and spring preload angle (also observed in Fig. 8): the constant thrust seen in Fig. 8(d) translates into a linear increase in thrust reduction with tip-speed ratio in Fig. 11(c). For the optimum case of $\theta = 290°$, the mean power reduction is close to zero over a range of λ between 5 to 6, and the corresponding mean thrust reduction varies from 17% to 24%. The reduction in thrust and power fluctuations is nearly 37% and 23%, respectively, at $\lambda = 6$. Previous studies [28,29] show that passive pitch is an effective technology in mitigating the mean and fluctuating thrust loads, while maintaining the rated power. In this study, we describe the effect of varying the preloads on the mean and fluctuating thrust and power. With a decrease in preload, passive pitch blades match the fixed pitch performance at lower λ, while mitigating the mean and fluctuating thrust loads across the entire range of tip-speed ratios considered. This suggests that even if we set a low preload such that the rated power is not matched, the thrust loads are reduced significantly, indicating that the structural loads experienced by the turbine are minimised. The reduction in thrust loads also has important implications for the hydrodynamic efficiency, which will be discussed further in Fig. 12.

Hydrodynamic efficiency is a measure of the useful power generated by the turbine as a proportion of the power removed from the flow (or the work done on the turbine support structure). Hydrodynamic efficiency is defined as:

$$\eta = \frac{Q\omega}{Tu_\infty} = \frac{C_P}{C_T} \tag{19}$$

The useful power generated by the turbine is $Q\omega$, whereas Tu_∞ is the power removed from the flow, which is the useful power generated plus hydrodynamic losses. If more power is removed from the flow, there is less energy available for any subsequent rows of turbines, and so the hydrodynamic efficiency is also referred to as the 'basin efficiency' [46]. Tu_∞ can also be interpreted as the thrust the rotor must withstand in order to generate a certain amount of power [47]. Looking at Fig. 12, it is seen that in general, passive pitch blades provide a comparatively greater hydrodynamic efficiency than rigid blades under design operating conditions at $u_\infty = 0.65$ m s^{-1}. In the case of fixed pitch blades, the maximum hydrodynamic efficiency is about 57% at $\lambda = 5$. For passive pitch blades with an optimum preload angle of $\theta = 290°$, η is nearly 66% at $\lambda = 5$. For passive pitch blades with a preload angle of $\theta = 168°$, this is about 79% at $\lambda = 4.5$. This, combined with the results from Fig. 8, indicates that a lower than optimal preload results in a loss of power but a gain in efficiency. The cases where the passive pitch gives a lower design-point efficiency than fixed pitch are those where the preload is set too high ($u_\infty = 0.5$ m s^{-1}, $\theta = 232°$ and $\theta = 290°$). An important finding from this study is that in a large tidal farm, even if we set a low preload that does not match the rated power, we significantly improve the hydrodynamic efficiency compared to turbines equipped with fixed pitch blades.

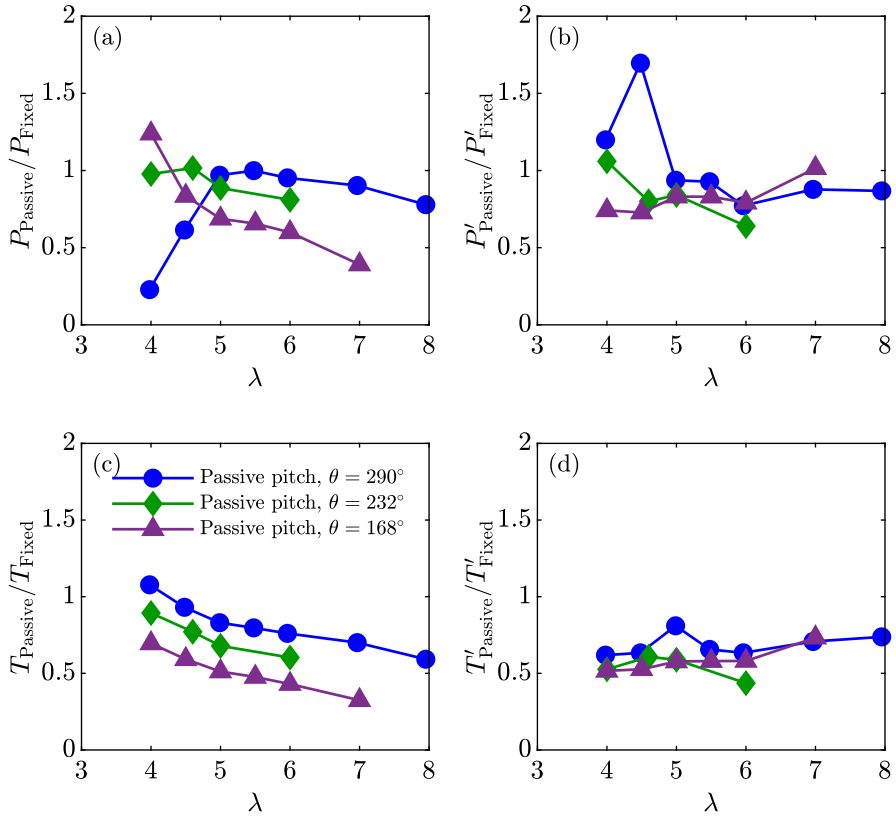

Fig. 11. Change in: (a) mean power, (b) power fluctuations, (c) mean thrust, and (d) thrust fluctuations of passive pitch blades with respect to fixed pitch blades at different tip-speed ratios and spring preload angles for an oncoming flow velocity of $u_\infty = 0.65$ m s^{-1}. The data are filtered with a low-pass Butterworth filter of 16 Hz. Change the figure as the ratio of loads and not the difference. Change label for readability.

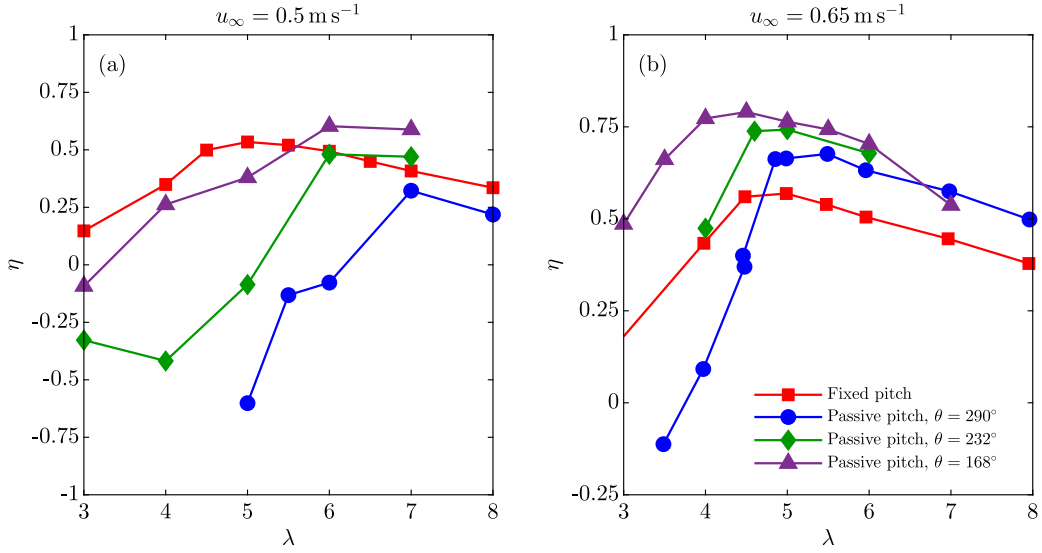

Fig. 12. Hydrodynamic efficiency of the turbine at different tip-speed ratio and flow velocities of (a) $u_\infty = 0.5$ m s^{-1}, and (b) $u_\infty = 0.65$ m s^{-1}.

As explained in Section 2.1, the inflow to the turbine had a degree of unsteadiness from two sources: the steady-state shear profile through which the turbine rotates, and a time-varying turbulence component of 6%–7%. Spectral analysis of the torque and thrust data were carried out to investigate the unsteady response of the passive pitch blades. The spectra are shown at low tip-speed ratio (around the design point) in Fig. 13 and at high tip-speed ratio ($\lambda \geq 6$) in Fig. 14. In all the plots, the spectrum from the fixed pitch turbine is shown in black, while the passive pitch data is shown in colour. Harmonics of rotor and blade passing frequency are marked as dotted lines. The one-per-revolution (1P) peak and its harmonics indicate differences in loading as the turbine rotates (e.g., due to the fact that the turbine is rotating through a sheared inflow).

At low tip-speed ratio (Fig. 13), $\lambda = 5$ and 5.5, there is little change to the torque spectra between the fixed and passive pitch turbines, but the thrust spectra (right-hand plots), show a reduction in frequency content at $f/\omega < 0.5$, suggesting that the passive pitch mechanism is effective at mitigating low frequency thrust fluctuations due to slow

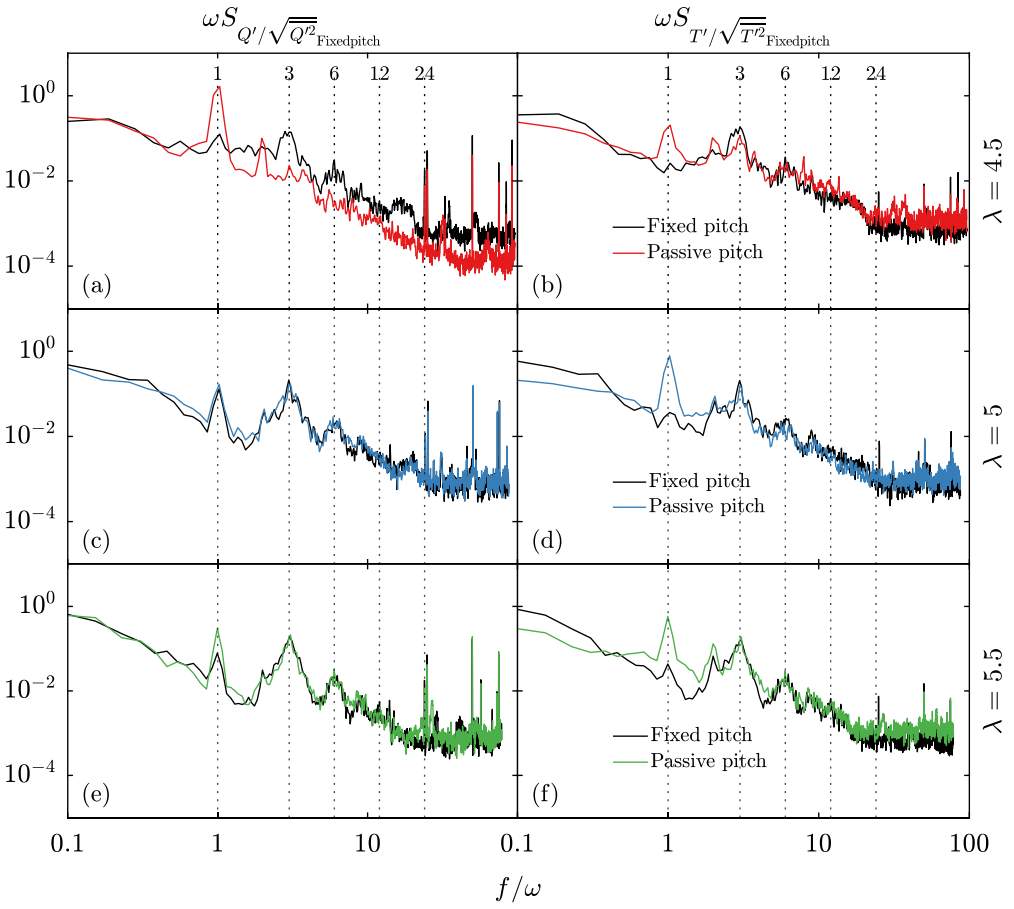

Fig. 13. Power spectral density of the torque and thrust fluctuations at low tip-speed ratio for $u_\infty = 0.65$ m s^{-1} and $\theta = 290°$: (a, (b) $\lambda = 4.5$, (c, (d) $\lambda = 5$, (e, (f) $\lambda = 5.5$.

changes in the oncoming flow velocity. This trend continues at high tip-speed ratio (Fig. 14), and there is some evidence at high λ that low frequency torque fluctuations are also reduced - this may be due to the reduction in mean torque at high λ (see Fig. 8(b)).

The spectra in Figs. 13 and 14 show that the current design is ineffective in mitigating high-frequency fluctuations. In most cases, there is a higher 1P peak in the data from the passive pitch turbine, and then the spectra tend to agree for $f/\omega > 2$. The increase in the 1P peak may be due to slight differences in blade weight or errors in spring preload between blades or other small inaccuracies in the pitch mechanism. In a full-size turbine, the pitch mechanism would be larger and therefore less prone to manufacturing/setup errors.

4.2. BEMT

4.2.1. Power and thrust

The fixed and passive-pitch blades have been numerically modelled using BEMT as outlined in Section 3. The test case modelled was that with an inflow velocity of $u_\infty = 0.65$ m s^{-1} with a pre-load of $\theta = 290°$ and a spring stiffness $\kappa = 0.31$ N m rad^{-1} which in the experiment saw the best match in recorded power between the fixed and passive-pitch turbines. The power, thrust and torque coefficients comparing fixed and passive pitch turbines can be seen in Figs. 15a and 15b, where the time-averaged BEMT results are plotted over those obtained during the experiment.

The experimental and numerical methods both agree in the location of peak C_P around $\lambda = 5$ to 6 for the fixed-pitch turbine. For the passively pitching turbines, both methods show an overall reduction of the power and thrust coefficients with increasing λ, which happens as a result of blades assuming new pitch positions with increasing loads. The BEMT results are also in agreement with the experiment as to the λ at which the fixed and passive turbines match performance, around $\lambda \approx 4.8$. The experimental data shows a match over a range of λ first around 4.8 and again close to 5.5, while the BEMT shows a single point of match, as expected from the theoretical model [26].

Generally, BEMT over-predicts the power and thrust at all λ. The results are presented in non-dimensional coefficient form, normalised using the nominal flow speed. However, previous characterisations of the experimental facility [30] have shown that flows measured using ADV are systematically lower than the reported nominal speed, with the difference at the tank centre being on the order of 4%. Power and thrust coefficients are functions of the third and second power of the velocity, respectively, where any uncertainty in the velocity would be greatly amplified in their calculations. Therefore, non-dimensionalisation of the measured loads using a corrected flow velocity 4% lower than nominal would see the experimental results translated upwards and show a better match with BEMT.

4.2.2. Power spectra and root-bending-moments

Similarities between the experiment and BEMT are seen in the power spectra of load fluctuation. Figs. 16a to 16c show the spectra of thrust and torque and root bending moment fluctuations, respectively, for $\lambda = 5.0$. The BEMT results show a visible 3P peak that is also seen in experimental spectra in Fig. 13, which arises from the contributions of individual blades. A 1P peak is also seen in the thrust and root-bending moment spectra of the passively pitching turbine. Experimentally, the lack of or a weak torque signal at 1P has also been observed by Gambuzza [28]. A systematically lower signal is seen in low frequencies for numerical and experimental results, implying that this configuration of passive pitch is most effective at alleviating loading arising from

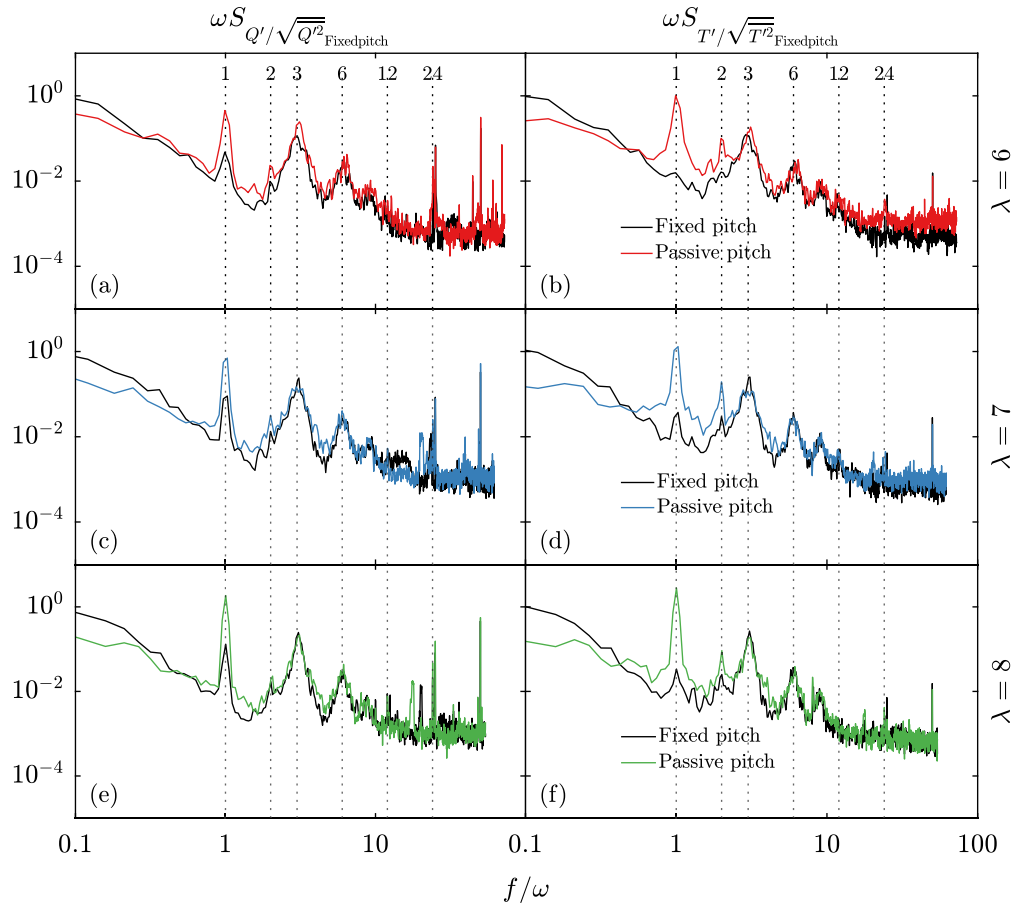

Fig. 14. Power spectral density of the torque and thrust fluctuations at high tip-speed ratio for $u_\infty = 0.65$ m s^{-1} and $\theta = 290°$: (a, (b) $\lambda = 6$, (c, (d) $\lambda = 7$, (e, (f) $\lambda = 8$.

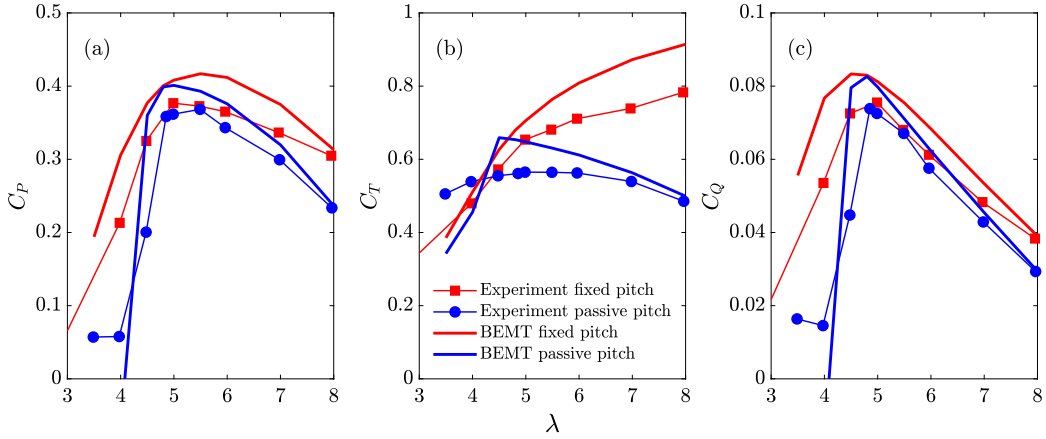

Fig. 15. Power, thrust and torque coefficients versus the tip-speed ratio for the experiment and the BEMT simulations.

slow-moving changes in the flow. At fight frequencies above 1P, the signals for the fixed and passive pitch turbines converge, pointing to the passive pitch system's effectiveness to be limited to timescales on the order of the rotor period.

Information about root bending moment loads, although not measured experimentally, can be investigated through BEMT. Fig. 16(c) shows the power spectrum of the flapwise bending moments M_{RBM} of a single blade, where similarities with the other spectra presented in this paper can be seen. Namely, mitigation of low-frequency fluctuations and a prominent peak at 1P which in total rotor loads is manifested as a peak at 3P from the contribution from all three blades. The reduction in peak height between the passive and fixed spectra is 67%.

The reductions in loading are given as ratios of standard deviation in Table 2. Root bending moment is seen to be reduced by the same order as the other quantities, by just over 20%.

4.2.3. Blade dynamics

The BEMT model offers additional insight into the dynamics of the turbines not captured directly in the experiment. For instance, the numerical output of the average angle of attack seen by the blade

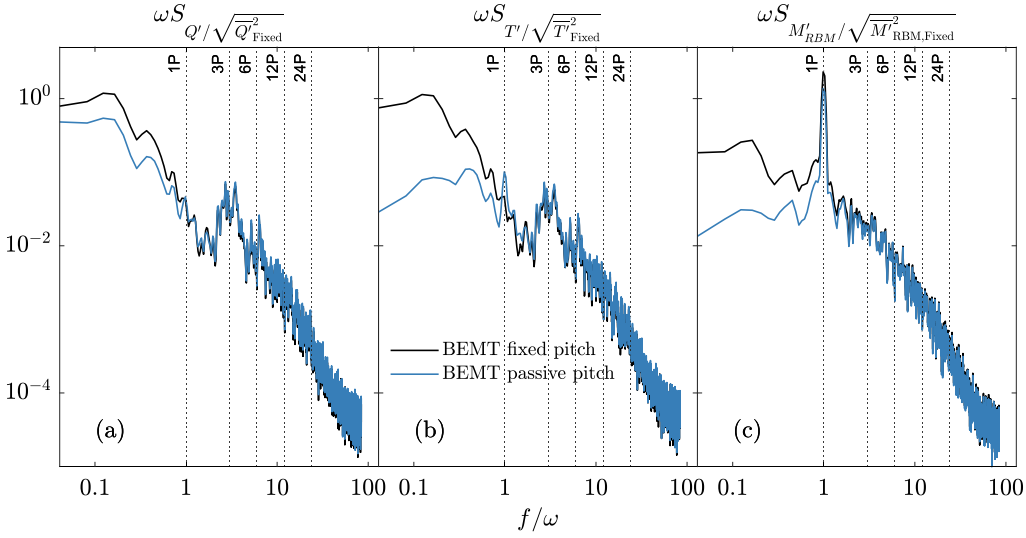

Fig. 16. PSD of BEMT torque, thrust and root bending moment fluctuations at $\lambda = 5.0$.

Table 2
Reduction in torque, thrust, and flapwise bending moment between passive and fixed pitch blades for both experiment and BEMT for $\lambda = 5.0$. The values are expressed as ratios of the standard deviation between passive and fixed turbines.

Variable	Experiment	BEMT
$Q'_{\text{pass}}/Q'_{\text{fix}}$	86.8%	82.6%
$T'_{\text{pass}}/T'_{\text{fix}}$	75.4%	68.9%
$M'_{\text{RBM,pass}}/M'_{\text{RBM,fix}}$	–	77.0%

can explain the significance of the choice of preload. Fig. 17(a) shows the blade-averaged angle of attack for both the fixed and passive turbines, while Fig. 17(b) shows the blade-averaged pitch angle for the passive-pitch turbine. It can be seen that the passively pitching blade experiences high angles of attack when $\lambda < 4.5$, signifying stall, while the angle of attack of the fixed pitch blade increases more gradually at low tip-speed ratios. At such conditions, the net hydrodynamic pitching moments are lower than the opposing moments from the preloaded spring, resulting in a blade nose-down motion (negative pitch) as the spring unwinds. This is indeed seen in Fig. 17(b), where at low λ the blade pitch is at very low values, eventually coming to rest at the hard stop set at $\beta = \pm 25°$. At the point where the hydrodynamic moments are exactly equal to the preload, the net-zero moments on the blade result in the blade remaining at its design position $\beta = 0°$. At $\beta = 0°$, the pitch and angle of attack are therefore equal to that of the fixed-pitch turbine, and so the average loads are also expected to match that of the fixed-pitch device.

A time series over 10 rotor periods τ_ω is seen in Fig. 18 for the turbine equipped with rigid and passive pitch blades. The series corresponds to the same flow conditions ($\lambda = 5$ and $u_\infty = 0.65\,\text{m}\,\text{s}^{-1}$) as used to produce the BEMT mean loads in Fig. 15, the spectra in Fig. 16, and the load reductions reported in Table 2. The unsteadiness in the freestream velocity u_∞ is seen to result in fluctuations in power and thrust. Here, the thrust and power curves are divided by the mean values of the fixed-pitch turbine. The passive pitch blade has a higher mean pitch angle than that of the fixed pitch blade, resulting in the lower mean thrust observed in Fig. 15. The rotor frequency is the dominant frequency of the pitch oscillations. This is consistent with the power spectrum of the blade root-bending-moment seen in Fig. 16(c), with a significant 1P peak.

4.2.4. Rated power and performance over a tidal cycle

The passive pitch system can be tuned to a given flow condition by, for instance, fixing a preload to the value of the hydrodynamic moments at target conditions. From previous work [26], it is also known that the location of the pitching axis can maximise either torque or thrust alleviation, and that the response of a blade to a change in loading will be dependent on the pitching axis location.

State-of-the-art tidal and wind turbines are capable of maintaining a constant power production at flow speeds above a rated condition u_R, by changing their rotational speed and blade pitch in order to lower the power coefficient of the devices. Such curtailment of power is a necessary safety feature used to ensure that devices operate within their rated specifications in the event of high flows, such as gusts or peaks within a tidal cycle. In this section, we extrapolate the results presented hitherto to demonstrate that constant power can be maintained by the turbine using the passive pitch mechanism paired with rotational speed control. Fig. 19 shows the load characteristics of a full-scale model of the turbine described in this paper, with a diameter of 24 m and a rated power of 1.1 MW at $u_R = 2.2\,\text{m}\,\text{s}^{-1}$. The time history of the flow speed is taken from field measurements around the deployment site of the European Marine Energy Centre, Orkney, UK, as part of the ReDAPT measurement campaign [48]. The three velocity components were obtained using ground-mounted acoustic Doppler current profilers at a sampling frequency of 1 Hz. Measurements were taken at a depth of 30 m, or 1.7 rotor radii above the seabed, taken as the hub height of the turbine. The complete tidal flow data set is openly available online [49].

Two tidal cycles with a period $\tau \approx 12.1$ h are considered. The time series of the magnitude of the velocity was averaged in bins of 120 s, and considered uniform over the rotor plane. Three cases are presented: (1) fixed pitch turbine; (2) passively pitching turbine with the original pitching axis from the experiments scaled to full scale; and (3) passively pitching turbine with an improved pitching axis, detailed below.

Below the rated flow speeds, the passive pitch turbine is considered equipped with a limiting pitch mechanism similar to that used in the experiments (see component I in Fig. 3). In the experiments, pitch variations of 25 ° were allowed in each direction to investigate the effect of extreme pitch values. However, in real applications, the limiting mechanism would allow only positive or slightly negative pitch values. Therefore, below the rated flow speeds, the pitch is the same as that of a fixed-pitch turbine. In these conditions, the turbine is operated at the peak C_P producing $\lambda = 5$.

As discussed in relation to Fig. 8, for a given preload, there exists an operating point (u_∞, λ), at which the power and thrust of a passive pitch turbine will match that of the fixed pitch device. For the full-scale turbine, this point has been chosen to be the rated flow speed of the device. Therefore, both the fixed and passively pitching turbines

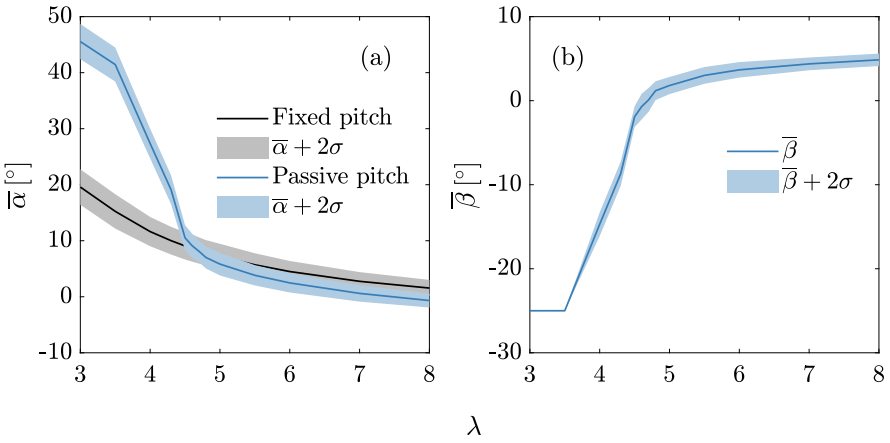

Fig. 17. Time and span averaged (a) angle of attack and (b) blade pitch from the BEMT model.

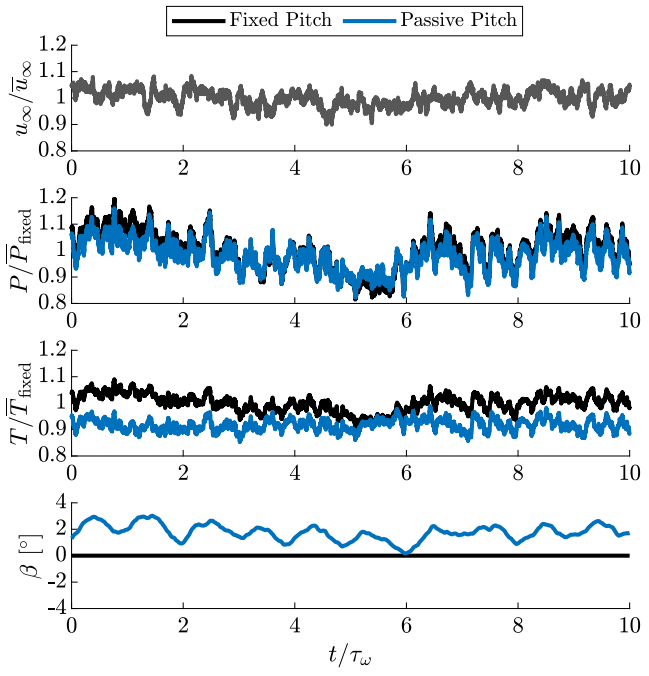

Fig. 18. Turbine response in loads and blade pitch shown against a varying flow speed as measured at hub height, taken for conditions $\overline{u}_\infty = 0.65$ m s^{-1} and $\lambda = 5.0$. The flow speed and loads are normalised with respect to the fixed-pitch mean, and the time axis by the rotor rotational period τ_ω.

assume the same rated rotational speed ω_R, and output the same rated power P_R and thrust T_R. Above rated speed, the passive pitch system results in a higher pitch than the fixed pitch value. At these conditions, the power is kept constant at the rated level by adjusting ω to values greater than rated.

The relationship between rotational speed and blade pitch is seen in Fig. 20, which demonstrates that power can be kept at P_R at flows above rated, over a range of turbine configurations.

In addition to the original axis used in the rest of this paper, results for an improved axis are shown. The new axis is such that it minimises the range of omega in the region $u_\infty > u_R$ needed to maintain constant power.

We can find a pitching axis that results in a pitch change satisfying $P(\beta_1, u_1, \omega_1) = P_R$, for any $\omega > \omega_R$, by imposing a balance of moments at both operating conditions. Ōtomo et al. [26] showed that a specific pitching axis position $\boldsymbol{r}_p = \{x_p, y_p\}$ can be found to keep any arbitrary blade-force component constant. The pitching position is a function of initial and final spring moments and hydrodynamic forces, and can be obtained for any initial $\{u_0, \omega_0\}$ and final $\{u_1, \omega_1\}$ set of flow and operating conditions. The method of Ōtomo et al. [26] applied to constant power production yields the expression for the axes as

$$x_p\left(F_{y,0} - F_{y,1}\right) - y_p\left(F_{x,0} - F_{x,1}\right) + \left(M_0 - M_1\right) = 0 \tag{20}$$

whose arguments are the force components ($F_{x,i}$) in the chord-wise and chord-normal directions, x and y, and quarter-chord moments (M_i). For any choice of the pitching axis coordinate x_p, a corresponding y_p can be obtained by rearranging Eq. (20). The specific pairing of $\{x_p, y_p\}$ obtained for each $\{u_1, \omega_1\}$ will affect the response of the turbine to unsteady flow. The choice of the location of the pitching axis is critical for optimising the design of the passive pitch system, but a detailed study on the effect of its position is beyond the scope of this paper. Instead, interested readers are pointed at Ōtomo et al. [26]. Here, the improved pitching axis location is at a chordwise coordinate corresponding to the quarter chord of the root profile, and 5 mm at model scale, and 90 mm at full scale (equivalent to 5% of the root chord length) towards the pressure side in the direction normal to the root section chord.

Three conclusions can be drawn from Fig. 19: Firstly, it demonstrates that multiple passive pitch configurations are capable of producing constant power at flow speeds above rated. The change in rotational speed from that used at rated conditions, ω_R, is also approximately three times lower for the passive pitch turbines than for the fixed pitch turbine. Secondly, peak thrust is also greatly reduced compared to a fixed pitch turbine. Lastly, the location of the pitching axis does have an effect on the change in ω needed for a constant power production, presented in greater detail in Fig. 21.

In earlier work by Gambuzza et al. [29], a comparison of an active and passive pitch system was presented as a first demonstration of power capping using passive pitch paired with a rotational speed controller. Despite constant power being achieved, the required increase in rotational speed was on the order of 20% with passive pitch. The significance of these new results is that a passively pitching system can be configured such that ω only varies on the order 3% when the flow speed surpasses the rated speed by 50%, given an appropriate choice of pitching axis. A passive pitch system is, therefore, capable of achieving most of the benefits of an active system, namely, maintaining constant power with significant thrust reduction, when coupled with a rotational speed controller.

5. Conclusions

In this paper, we have investigated the effect of spring preload, tip-speed ratio, and incoming flow velocity on the performance of a tidal

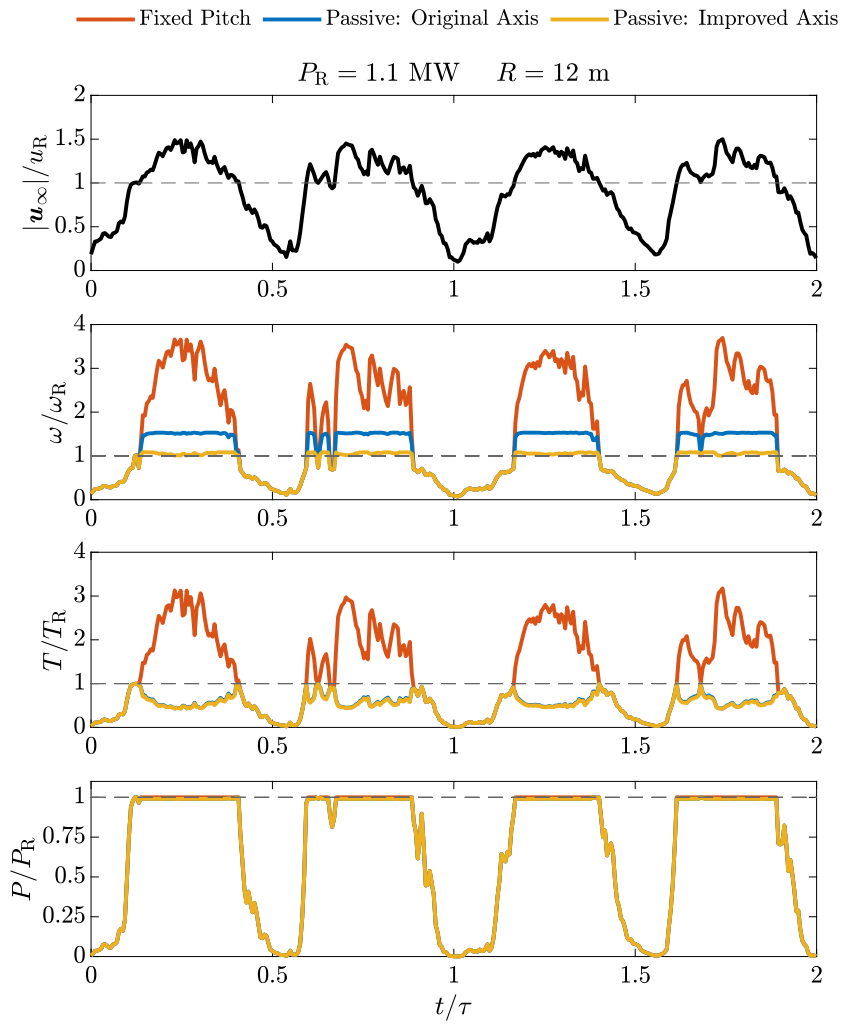

Fig. 19. Simulated operations of a full-scale tidal turbine with fixed and passive pitch over a real, measured tidal flow with a tidal cycle $\tau \approx 12.1$ h, and $u_R = 2.2$ m s^{-1}.

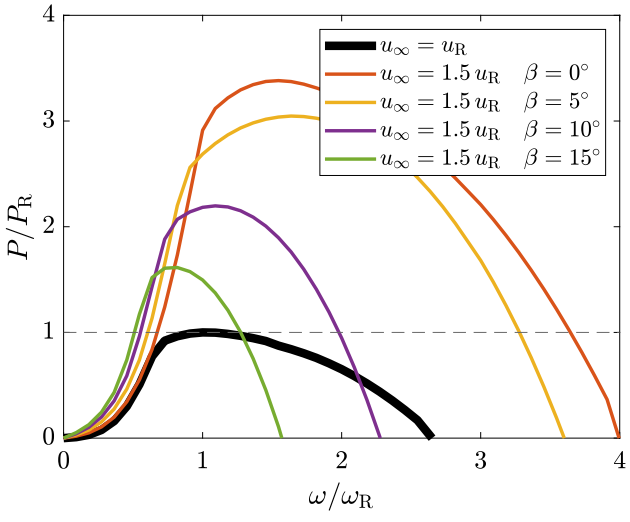

Fig. 20. Effect of rotational speed and blade pitch on power output at flow velocities above rated.

turbine equipped with three independent, passively-pitching blades. The results presented in this work include the outputs from BEMT and from experiments conducted in a circular wave and current tank. The main findings from the paper are summarised below.

For a given flow speed, one can design a spring such that the power and thrust of a passive pitch turbine are the same as those of a fixed pitch turbine for at least one tip-speed ratio and flow velocity. With decreasing preload angle, the power varies by a small amount while the mean thrust decreases. For a passive pitch turbine, there is a sudden drop in performance at low-λ, due to the change in pitch causing the blade to stall. Above this minimum λ, the passive pitch turbine matches the fixed pitch power for $\lambda \simeq 4.5-6$, while the thrust remains constant, and thus the hydrodynamic efficiency is increased near the turbine design point.

Spectral analysis of the thrust and torque fluctuations indicates that passive pitch is an effective mechanism in mitigating low-frequency fluctuations, such as those happening due to slow changes in the oncoming flow velocity. The passive pitch turbine provides a significantly higher hydrodynamic efficiency: 78% compared to 55% for the fixed pitch turbine at design conditions.

The responsiveness of the system can also be used for power capping purposes when paired with a rotational speed controller, which is common in modern turbines. Specifically, we demonstrated that a turbine equipped with passive pitch and speed control results in the same energy yield over a tidal cycle as a turbine equipped with active pitch control.

Finally, we show that a low-order numerical model based on blade element momentum theory is capable of capturing the time-average

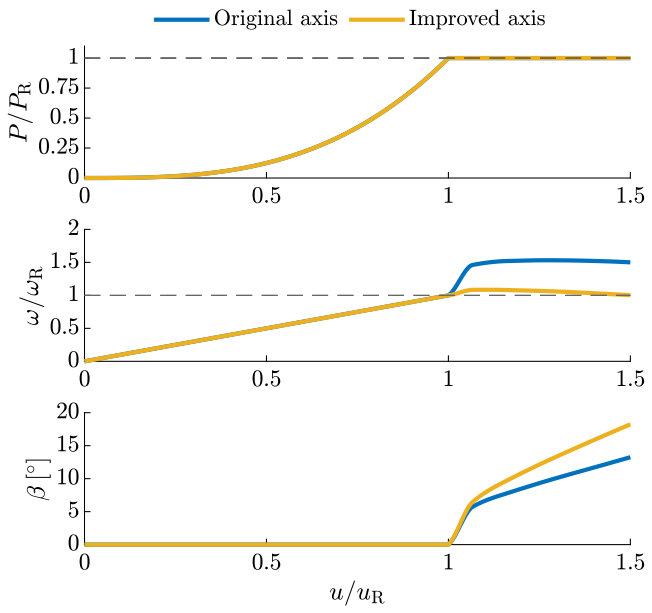

Fig. 21. Characteristics of a passive pitch system with an improved pitching axis location, showing the range of ω and β changes needed to maintain power at rated level over a range of flow speed. Below rated speed, the pitch is fixed.

and dynamic performance (including high frequency fluctuations) of experimental pitching turbines, and is a suitable tool for prototyping and analysing passive pitch systems.

These results demonstrate that passive pitch systems can be used to mitigate unsteady load fluctuations and can replace active pitch systems to increase system reliability. We have also shown that an efficient passive pitch system can be designed with an unsteady BEMT model. However, the present results are limited to a fixed pitching axis. Ōtomo et al. [26] showed that the performance of the passive pitch system depends on the pitching axis position, but experimental work exploring different pitching axes is yet to be undertaken. While the pitching axis in the present tests differs from that adopted by the two previous tests of Gambuzza et al. [28,29], the different pitching systems, blade geometries and flow conditions do not allow a consistent comparison on the effect of the pitching axis location. Therefore, future work should focus on the effect of the pitching axis location. These three experimental works also explore only a small range of flow velocities compared to those experienced by a full-scale turbine. The difference between the two speeds tested in this work is only 30%, while a full-scale turbine operates in flow speeds that vary by up to 200% from the rated speed. While our BEMT simulations show that this range of flow speeds can be managed by a well-designed passive pitch system, this has yet to be experimentally demonstrated. Finally, the effect of the friction of a bearing on the passive pitch system, particularly for a water-tight sealed bearing, should be carefully investigated. In fact, while some level of friction was present in the present tests and in the previous ones [28,29], the passive pitch system was wet for all of these tests, and no attempt was made to protect it with watertight bearings. If one wants to adopt a dry passive pitch system at full scale, then the effect of the bearing friction should be carefully verified.

Data underpinning the present results are available on the Edinburgh DataShare at the hyperlink [to be provided prior to publication].

CRediT authorship contribution statement

Puja Sunil: Writing – original draft, Visualization, Investigation, Formal analysis, Data curation. **Kuba Frankowski:** Writing – original draft, Visualization, Validation, Software, Methodology, Investigation, Formal analysis, Data curation. **Anna M. Young:** Writing – review & editing, Supervision, Resources, Project administration, Methodology, Funding acquisition, Conceptualization. **Michael O'Sullivan:** Methodology. **Edward D. McCarthy:** Supervision, Resources, Methodology, Funding acquisition, Conceptualization. **Riccardo Broglia:** Supervision. **Ignazio Maria Viola:** Supervision, Resources, Project administration, Methodology, Funding acquisition, Conceptualization.

Declaration of competing interest

The authors declare the following financial interests/personal relationships which may be considered as potential competing interests: Ignazio Maria Viola, Edward McCarthy, Anna Young, Puja Sunil, Kuba Frnkowski, and Michael O'Sullivan report financial support was provided by the Engineering and Physical Sciences Research Council. Michael O'Sullivan reports financial support was provided by the Energy Technology Partnership. Ignazio Maria Viola has patent #PCT/GB2024/050216 issued to University of Edinburgh. Edward D. McCarthy and Ignazio Maria Viola have patent #PCT/GB2024/050216 licensed to University of Edinburgh. If there are other authors, they declare that they have no known competing financial interests or personal relationships that could have appeared to influence the work reported in this paper.

Acknowledgements

This work was supported by the UK Engineering and Physical Sciences Research Council (EPSRC) through the grant 'Morphing-Blades: New-Concept Turbine Blades for Unsteady Load Mitigation' [EP/V009443/1], as well as the Impact Acceleration Account 'Fatigue modelling/testing of advanced morphing tidal turbine blades.' KF was supported by the EPSRC Centre for Doctoral Training in Wind and Marine Energy and Structures [EP/S023801/1] and MOS by a scholarship funded by the Energy Technology Partnership.

References

[1] Ocean Energy Systems, Ocean energy and net zero: An international roadmap to develop 300GW of ocean energy by 2050, 2023, https://www.ocean-energy-systems.org/publications/oes-documents/market-policy-/document/ocean-energy-and-net-zero-an-international-roadmap-to-develop-300gw-of-ocean-energy-by-2050/.

[2] S.T. Harvey, X. Chen, D. Rowe, J. McNaughton, C. Vogel, K. Bhavsar, T. Allsop, J. Gilbert, H. Mullings, T. Stallard, et al., Tidal turbine benchmarking project: Stage I- steady flow experiments, in: The 15th European Wave and Tidal Energy Conference, 2023, http://dx.doi.org/10.36688/ewtec-2023-553.

[3] T.A. Adcock, S. Draper, G.T. Houlsby, A.G. Borthwick, S. oğluSena, The available power from tidal stream turbines in the Pentland Firth, Proc. R. Soc. A: Math. Phys. Eng. Sci. 469 (2157) (2013) 20130072, http://dx.doi.org/10.1098/rspa.2013.0072.

[4] G.T. Scarlett, B. Sellar, T. Van Den Bremer, I.M. Viola, Unsteady hydrodynamics of a full-scale tidal turbine operating in large wave conditions, Renew. Energy 143 (2019) 199–213, http://dx.doi.org/10.1016/j.renene.2019.04.123.

[5] G.T. Scarlett, I.M. Viola, Unsteady hydrodynamics of tidal turbine blades, Renew. Energy 146 (2020) 843–855, http://dx.doi.org/10.1016/j.renene.2019.06.153.

[6] P. Ouro, T. Nishino, Performance and wake characteristics of tidal turbines in an infinitely large array, J. Fluid Mech. 925 (2021) A30, http://dx.doi.org/10.1017/jfm.2021.692.

[7] J. McNaughton, B. Cao, A. Nambiar, T. Davey, C.R. Vogel, R.H. Willden, Constructive interference effects for tidal turbine arrays, J. Fluid Mech. 943 (2022) A38, http://dx.doi.org/10.1017/jfm.2022.454.

[8] E.A. Bossanyi, The design of closed loop controllers for wind turbines, Wind. Energy: Int. J. Prog. Appl. Wind. Power Convers. Technol. 3 (3) (2000) 149–163, http://dx.doi.org/10.1002/we.34.

[9] A. El Yaakoubi, A. Bouzem, R. El Alami, N. Chaibi, O. Bendaou, Wind turbines dynamics loads alleviation: Overview of the active controls and the corresponding strategies, Ocean Eng. 278 (2023) 114070, http://dx.doi.org/10.1016/j.oceaneng.2023.114070.

[10] T.K. Barlas, W. Van Wingerden, A. Hulskamp, G.M. van Kuik, H.N. Bersee, Smart dynamic rotor control using active flaps on a small-scale wind turbine: aeroelastic modeling and comparison with wind tunnel measurements, Wind. Energy 16 (8) (2013) 1287–1301, http://dx.doi.org/10.1002/we.1560.

[11] M.A. Lackner, G. van Kuik, A comparison of smart rotor control approaches using trailing edge flaps and individual pitch control, Wind. Energy: Int. J. Prog. Appl. Wind. Power Convers. Technol. 13 (2–3) (2010) 117–134, http://dx.doi.org/10.1002/we.353.
[12] A. Zaki, M. Abdelrahman, S.S. Ayad, O. Abdellatif, Effects of leading edge slat on the aerodynamic performance of low Reynolds number horizontal axis wind turbine, Energy 239 (2022) 122338, http://dx.doi.org/10.1016/j.energy.2021.122338.
[13] A.M. Cooperman, R. Chow, C. Van Dam, Active load control of a wind turbine airfoil using microtabs, J. Aircr. 50 (4) (2013) 1150–1158, http://dx.doi.org/10.2514/1.C032083.
[14] L.O. Bernhammer, G.A. van Kuik, R. De Breuker, Fatigue and extreme load reduction of wind turbine components using smart rotors, J. Wind Eng. Ind. Aerodyn. 154 (2016) 84–95, http://dx.doi.org/10.1016/j.jweia.2016.04.001.
[15] A.M. Young, J.R. Farman, R.J. Miller, Load alleviation technology for extending life in tidal turbines, in: Progress in Renewable Energies Offshore: Proceedings of the 2nd International Conference on Renewable Energies, 2016, RENEW2016, Taylor & Francis Books Ltd, 2016, pp. 521–529, http://dx.doi.org/10.17863/CAM.99753.
[16] S.J. Johnson, J.P. Baker, C. Van Dam, D. Berg, An overview of active load control techniques for wind turbines with an emphasis on microtabs, Wind. Energy: Int. J. Prog. Appl. Wind. Power Convers. Technol. 13 (2–3) (2010) 239–253, http://dx.doi.org/10.1002/we.356.
[17] U. Cordes, B. Lambie, K. Hufnagel, H. Spiegelberg, G. Kampers, C. Tropea, The adaptive camber concept—A passive approach for gust load alleviation on wind turbines, Wind. Energy 21 (9) (2018) 732–744, http://dx.doi.org/10.1002/we.2190.
[18] S. Hoerner, S. Abbaszadeh, O. Cleynen, C. Bonamy, T. Maître, D. Thévenin, Passive flow control mechanisms with bioinspired flexible blades in cross-flow tidal turbines, Exp. Fluids 62 (2021) 1–14, http://dx.doi.org/10.1007/s00348-021-03186-8.
[19] K. Van Ness, A. Aliseda, B. Polagye, Experimental comparison of passive adaptive blade pitch control strategies for an axial-flow current turbine, J. Ocean. Eng. Mar. Energy 10 (1) (2024) 105–123, http://dx.doi.org/10.1007/s40722-023-00302-0.
[20] C.L. Bottasso, A. Croce, F. Gualdoni, P. Montinari, Load mitigation for wind turbines by a passive aeroelastic device, J. Wind Eng. Ind. Aerodyn. 148 (2016) 57–69, http://dx.doi.org/10.1016/j.jweia.2015.11.001.
[21] A. Arredondo-Galeana, A.M. Young, A.S. Smyth, I.M. Viola, Unsteady load mitigation through a passive trailing-edge flap, J. Fluids Struct. 106 (2021) 103352, http://dx.doi.org/10.1016/j.jfluidstructs.2021.103352.
[22] R.E. Murray, S. Ordonez-Sanchez, K.E. Porter, D.A. Doman, M.J. Pegg, C.M. Johnstone, Towing tank testing of passively adaptive composite tidal turbine blades and comparison to design tool, Renew. Energy 116 (2018) 202–214, http://dx.doi.org/10.1016/j.renene.2017.09.062.
[23] I.M. Viola, G. Pisetta, W. Dai, A. Arredondo-Galeana, A.M. Young, A.S.M. Smyth, Morphing Blades: Theory and Proof of Principles, Internat. Marine Energy J. 5 (2) (2022) 183–193, http://dx.doi.org/10.36688/imej.5.183-193.
[24] G. Pisetta, R. Le Mestre, I.M. Viola, Morphing blades for tidal turbines: A theoretical study, Renew. Energy 183 (2022) 802–819, http://dx.doi.org/10.1016/j.renene.2021.10.085.
[25] W. Dai, R. Broglia, I.M. Viola, Mitigation of rotor thrust fluctuations through passive pitch, J. Fluids Struct. 112 (2022) 103599, http://dx.doi.org/10.1016/j.jfluidstructs.2022.103599.
[26] S. Ōtomo, S. Gambuzza, Y. Liu, A.M. Young, R. Broglia, E.D. McCarthy, I.M. Viola, A general framework for the design of efficient passive pitch systems, Phys. Fluids 36 (6) (2024) http://dx.doi.org/10.1063/5.0212626.
[27] Y. Liu, R. Broglia, A.M. Young, E.D. McCarthy, I.M. Viola, Unsteady load mitigation through passive pitch, J. Fluids Struct. 131 (2024) 104216, http://dx.doi.org/10.1016/j.jfluidstructs.2024.104216.
[28] S. Gambuzza, G. Pisetta, T. Davey, J. Steynor, I.M. Viola, Model-scale experiments of passive pitch control for tidal turbines, Renew. Energy 205 (2023) 10–29, http://dx.doi.org/10.1016/j.renene.2023.01.051.
[29] S. Gambuzza, P. Sunil, M. Felli, A.M. Young, R. Broglia, E.D. McCarthy, I.M. Viola, Power and thrust control by passive pitch for tidal turbines, Renew. Energy 239 (2025) 121921, http://dx.doi.org/10.1063/5.0212626.
[30] D.R. Noble, Combined Wave-Current Scale Model Testing at Flowave (Ph.D. thesis), University of Edinburgh, 2018, URL http://hdl.handle.net/1842/31170.
[31] S. Gambuzza, G. Pisetta, T. Davey, J. Steynor, I.M. Viola, Model-scale experiments of passive pitch control for tidal turbines, Renew. Energy 205 (2023) 10–29, http://dx.doi.org/10.1016/j.renene.2023.01.051.
[32] M. Tanaka, G. Girard, R. Davis, A. Peuto, N. Bignell, Recommended table for the density of water between 0 C and 40 C based on recent experimental reports, Metrologia 38 (4) (2001) 301, http://dx.doi.org/10.1088/0026-1394/38/4/3.
[33] L. Korson, W. Drost-Hansen, F.J. Millero, Viscosity of water at various temperatures, J. Phys. Chem. 73 (1) (1969) 34–39, http://dx.doi.org/10.1021/j100721a006.
[34] P.J. Moriarty, A.C. Hansen, Aerodyn Theory Manual, Tech. Rep., National Renewable Energy Lab., Golden, CO (US), 2005, http://dx.doi.org/10.2172/15014831.
[35] B. Jonkman, R.M. Mudafort, A. Platt, E. Branlard, M. Sprague, jjonkman, HaymanConsulting, G. Vijayakumar, M. Buhl, H. Ross, P. Bortolotti, M. Masciola, S. Ananthan, M.J. Schmidt, J. Rood, rdamiani, nrmendoza, sinolonghai, M. Hall, ashesh2512, kshaler, K. Bendl, pschuenemann, psakievich, ewquon, mattrphillips, N. Kusuno, alvarogonzalezsalcedo, T. Martinez, rcorniglion, Openfast/Openfast: OpenFAST v3.1.0, Zenodo, 2022, http://dx.doi.org/10.5281/zenodo.6324288.
[36] C.N.H. Lock, Airplane Propellers, Springer, Berlin, Germany, 1935, http://dx.doi.org/10.1007/978-3-642-91487-4_3.
[37] K. Frankowski, xfoil2ad: A tool for automating the creation of AeroDyn v15/OpenFAST compatible aerodynamic polars using XFOIL, 2024, URL https://github.com/yeastem/xfoil2ad/.
[38] M. Drela, XFOIL: An analysis and design system for low Reynolds number airfoils, in: Low Reynolds Number Aerodynamics: Proceedings of the Conference Notre Dame, Indiana, USA, 5–7 June 1989, Springer, 1989, pp. 1–12, http://dx.doi.org/10.1007/978-3-642-84010-4_1.
[39] S.A. Ning, AirfoilPreppy: A Python module for preprocessing and evaluating aerodynamic airfoil data, 2019, URL https://github.com/WISDEM/AirfoilPreppy.
[40] J. van Ingen, The eN method for transition prediction. Historical review of work at TU Delft, in: 38th Fluid Dynamics Conference and Exhibit, http://dx.doi.org/10.2514/6.2008-3830.
[41] MathWorks, MATLAB Version: 9.13.0 (R2022b), The MathWorks Inc., Natick, Massachusetts, United States, 2022, URL https://www.mathworks.com.
[42] T. Theodorsen, General Theory of Aerodynamic Instability and the Mechanism of Flutter, Tech. Rep., 1979, URL https://ntrs.nasa.gov/citations/19800006788?utm_source=chatgpt.com.
[43] K. Frankowski, P. Sunil, M. O'Sullivan, A.M. Young, R. Broglia, E.D. McCarthy, I.M. Viola, Numerical modelling of friction in passively pitching blades for tidal turbines, in: Proceedings of the 11th International Conference on Computational Methods in Marine Engineering, 2025, http://dx.doi.org/10.36688/ewtec-2025-756.
[44] G. Pisetta, Passive Load Alleviation by Morphing Blades for Tidal Turbines, The University of Edinburgh, 2022, http://dx.doi.org/10.7488/ERA/2623.
[45] B.J. Jonkman, Turbsim User's Guide, Tech. Rep., National Renewable Energy Lab.(NREL), Golden, CO (United States), 2006, http://dx.doi.org/10.2172/965520.
[46] T.A. Adcock, S. Draper, R.H. Willden, C.R. Vogel, The fluid mechanics of tidal stream energy conversion, Annu. Rev. Fluid Mech. 53 (2021) 287–310, http://dx.doi.org/10.1146/annurev-fluid-010719-060207.
[47] A. Young, A. Smyth, V. Bajpai, R. Augarde, J. Farman, C. Sequeira, Improving tidal turbine efficiency using winglets, 2019, URL https://researchportal.bath.ac.uk/en/publications/improving-tidal-turbine-efficiency-using-winglets.
[48] B. Sellar, G. Wakelam, D. Sutherland, D. Ingram, V. Venugopal, Characterisation of tidal flows at the European marine energy centre in the absence of ocean waves, Energies 11 (1) (2018) 176, http://dx.doi.org/10.3390/en11010176, URL https://www.mdpi.com/1996-1073/11/1/176.
[49] B. Sellar, C. Old, D. Ingram, Field-Measurements Aligned to the Implementation of a Tidal Energy Converter's Power Performance Assessment, IEC 62600-200 PPA Type B, University of Edinburgh. School of Engineering, 2022, http://dx.doi.org/10.7488/DS/3449.